České vysoké učení technické v Praze
Fakulta jaderná a fyzikálně inženýrská

Katedra fyziky
Obor: Experimentální jaderná a částicová fyzika

Charakterizace křemíkového senzoru ALPIDE

Characterization of the ALPIDE silicon sensor

Výzkumný úkol

Vypracovala: Bc. Valentina Raskina
Vedoucí práce: RNDr. Filip Křížek, Ph.D.
Rok: 2018

Prohlášení

Prohlášuji, že jsem svůj výzkumný úkol vypracovala samostatně a použila jsem pouze podklady (literaturu, projekty, SW atd.) uvedené v přiloženém seznamu.

Nemám závažný důvod proti použití tohoto školního díla ve smyslu §60 Zákona č. 121/2000 Sb., o právu autorském, o právech souvisejících s právem autorským a o změně některých zákonů (autorský zákon).

V Praze dne .....

.....
Bc. Valentina Raskina

Acknowledgment

I would like to express my sincere gratitude to my supervisor, RNDr. Filip Křížek, Ph.D., for his patient guidance, great support, encouragement, invaluable advices and his time. I am extremely lucky to have a supervisor who cares so much about my work.

Bc. Valentina Raskina

Název práce:
Charakterizace křemíkového senzoru ALPIDE

Autor: Bc. Valentina Raskina

Obor: Experimentální jaderná a částicová fyzika
Druh práce: Výzkumný úkol

Vedoucí práce: RNDr. Filip Křížek, Ph.D.
Ústav jaderné fyziky AV ČR, v.v.i.

Abstrakt: Experiment ALICE v CERN připravuje inovaci svého vnitřního dráhového detektoru. Tento detektor bude sestávat ze sedmi koncentrických vrstev křemíkových senzorů ALPIDE, založených na technologii MAPS. S tímto projektem je spojena celá řada testovacích studií, kdy se sleduje odezva senzorů ALPIDE na částice ionizujícího záření. K testování radiační odolnosti senzorů používáme cyklotron U-120M, který se nachází v Ústavu jaderné fyziky AV ČR v Řeži. Hlavním cílem této práce je vyhodnotit výsledky radiačních testů senzoru ALPIDE prováděných na cyklotronu U-120M.

Klíčová slova: ALICE ITS upgrade, polovodičové detektory, radiační poškození v polovodičových detektorech, ALPIDE, MAPS, cyklotron

Title:
Characterization of the ALPIDE silicon sensor

Author: Bc. Valentina Raskina

Supervisor: RNDr. Filip Křížek, Ph.D.
Ústav jaderné fyziky AV ČR, v.v.i.

Abstract: The experiment ALICE at CERN plans to upgrade its Inner Tracking System detector. This detector will consist of seven concentric cylindrical layers of silicon sensors ALPIDE based on the MAPS technology. This project encompasses wide range of tests which characterize response of ALPIDE sensors to ionization radiation. For radiation hardness tests of this sensor the cyclotron U-120M of the Nuclear Physics Institute of the Czech Academy of Sciences in Řež is used. The main goal of this thesis is to analyze the results of radiation hardness tests of ALPIDE sensors carried out at the cyclotron U-120M.

Key words: ALICE ITS upgrade, semiconductor detectors, radiation damage in semiconductors, ALPIDE, MAPS, cyclotron

Contents

Introduction

ALICE (A Large Ion Collider Experiment) [1] is a heavy-ion detector at the CERN Large Hadron Collider (LHC) [2]. It is designed to study strongly interacting matter in the regime of high-energy densities and temperatures using proton-proton, proton-nucleus and nucleus-nucleus collisions. In this regime, nuclear matter undergoes transition to the state called Quark-gluon plasma (QGP) [3], consisting of deconfined color charge particles, quarks and gluons [4, 5]. Information about QGP properties can be obtained indirectly, e.g. from measurements of particle multiplicities, transverse momentum spectra, azimuthal distribution of particles with respect to reaction plane and from jet quenching measurements [5, 6]. Multiplicity of final state particles created in a heavy-ion collision is high and can reach couple of thousands of particles per unit of pseudorapidity in midrapidity [7]. ALICE was therefore designed as a multi-purpose detector which is able to provide efficient track reconstruction and particle identification in high-multiplicity environment. The ALICE detector consists of a central barrel, a forward muon spectrometer, and a set of small detectors for triggering and event characterization. ALICE allows to study hadrons, electrons, muons, photons and jets. The schematic drawing of the current ALICE detector is shown in Figure 1.

Run3 is a new period of data taking after the Second Long LHC shutdown (LS2). The LS2 will take place in 2019–2020 and is intended for the LHC upgrade. ALICE expects that in Run3, the LHC will deliver 100 times higher luminosity with respect to previous data taking periods. To be able to accomplish the physics program planned for Run 3, ALICE will undergo an upgrade during the LS2 [8]. The main goals of the ALICE physics program for Run3 are summarized in the letter of intent from 2014 [9]. ALICE wants to:

- measure open heavy flavor (HF) hadrons and quarkonia down to zero p_T to gain more information about HF thermalization and temperature evolution of the QGP,
- measure vector mesons and low-mass di-electrons which carry information about chiral symmetry restoration and thermal radiation from the QGP,
- perform high-precision measurements of the light nuclei, anti-nuclei, and hyper-nuclei production.

Since none of these observables provides a suitable trigger signature, ALICE plans to take minimum bias events in a continuous readout mode. The ALICE upgrade can be described as follows. Starting from the center of ALICE, there will be a new silicon Inner Tracking System (ITS), see Figure 2. In front of the muon arm absorber there will be a new forward muon tracker with five layers of silicon sensors which will improve resolution in the muon arm. The Time Projection Chamber (TPC) will upgrade its readout system to allow continuous readout, the gating grid in TPC will be replaced with a stack of GEM foils. They will provide electron multiplication and prevent backward flow of positive ions back to TPC [10]. The current forward detectors T0 and V0 which are used for centrality selection, event plane reconstruction and triggering will be replaced by a new Forward Interaction Trigger (FIT) detector [11]. Other detector upgrades concern readout electronics.

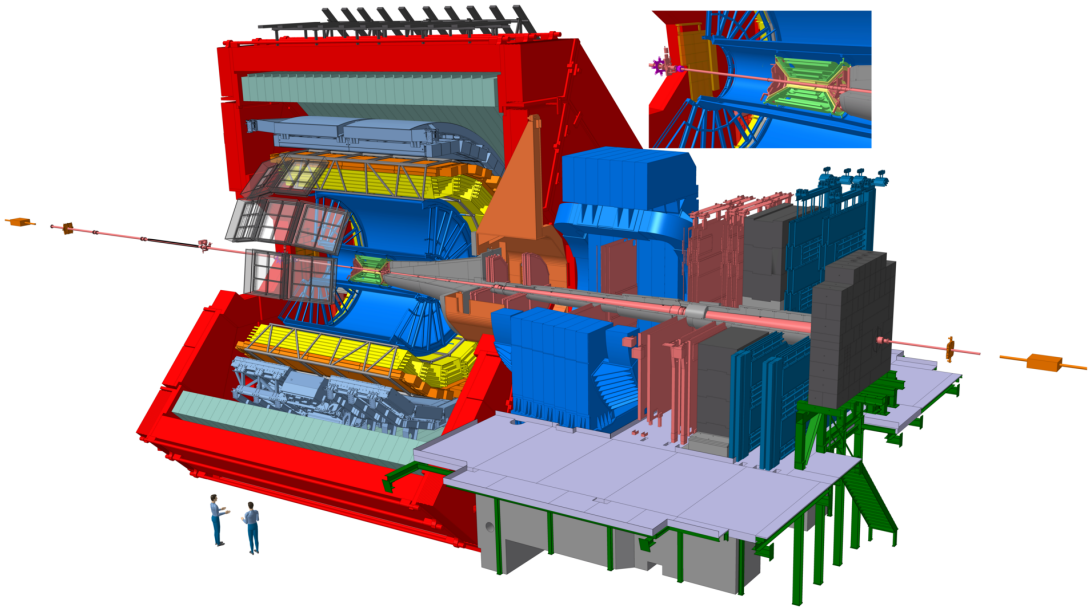

Figure 1: The current ALICE detector, taken from [12]. ALICE consists of central barrel and muon spectrometer. The current ITS is in the center of central barrel and is colored green, Its zoomed sketch is in the upper right corner. ITS is surrounded by TPC detector, colored blue. Red part of detector is a solenoid, which creates magnetic field 0.5 T

This work is related to the upgrade of the ITS. In particular, it deals with radiation hardness of ITS pixel sensor ALPIDE and its characterization. The new ALICE ITS will consist of seven concentric cylindrical layers of ALPIDE chips, 4 layers in the Outer Barrel (OB) and 3 layers in the Inner Barrel (IB). The expected Total Ionization Dose (TID) that an IB sensor will get during Run 3 is 270 krad and the expected Non-Ionizing Energy-Loss (NIEL) is 1.7 $\times 10^{12}$ 1 MeV$\cdot n_{eq} \cdot cm^{-2}$. The project goal however assumes that the ALPIDE chip should

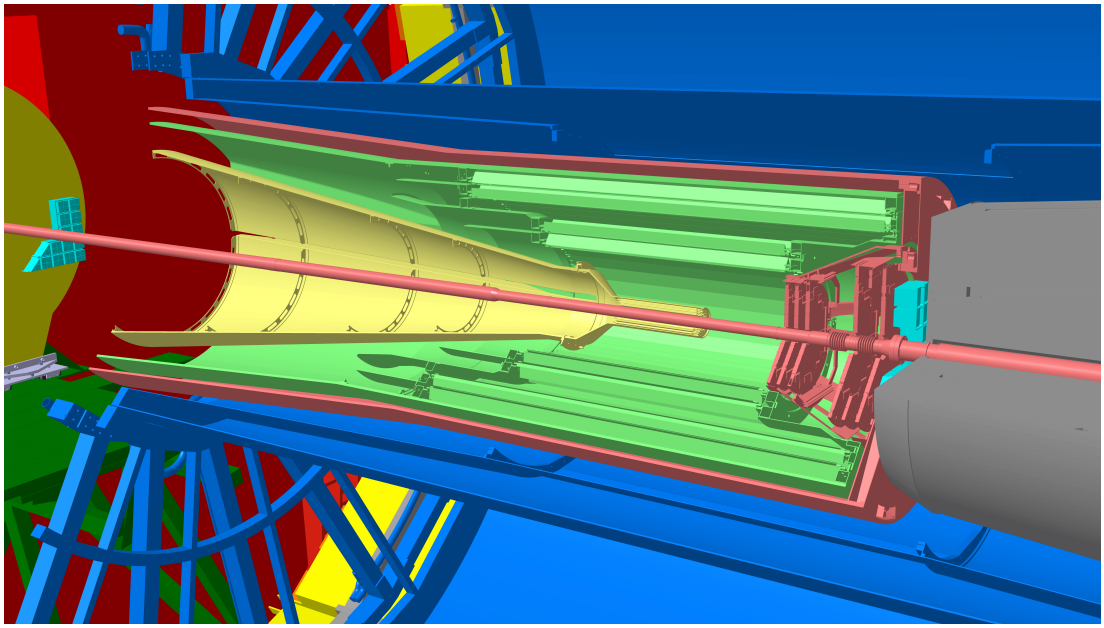

Figure 2: Central part of the ALICE detecor after the upgrade, taken from [12]. The new ITS is colored green and yellow. The MFT is colored pink, the FIT is light blue and is installed on the left and the right side of ITS.

sustain ten times higher radiation loads [8].

The first goal of this thesis is to investigate radiation hardness of the ALPIDE sensor using 30 MeV proton beam provided by the U-120M cyclotron of the Nuclear Physics Institute of the Czech Academy of Sciences in Řež. The second goal is to analyze data from ALPIDE beam tests done at the CERN Proton Synchrotron (PS).

This research work is organized as follows. Chapter 1 gives a brief introduction to semiconductor detectors and problematics of their radiation damage. Chapter 2 describes the upgraded ITS and the ALPIDE sensor. The third chapter is dedicated to experimental setup for radiation hardness tests of ALPIDE sensors at the U-120M cyclotron in Řež. The final chapter presents the analysis of irradiations at the U-120M cyclotron.

Chapter 1

Semiconductor detectors

Semiconductor detectors are solid-state detectors, based on crystalline semiconductor material. The most commonly used semiconductor materials are silicon (Si), germanium (Ge), gallium arsenide (GaAs) or cadmium-zinc-telluride (CdZnTe). The operating principle of semiconductor detectors is that ionizing radiation passing through the sensitive area of detector (semiconductor) creates electron-hole pairs which can be moved and collected by electric field. The energy needed to create an electron-hole pair in semiconductor material is very small $\approx$ 3.6 eV for Si [13], which is a primary advantage of semiconductors when compared to a gas detector where the ionization energy is order of magnitude higher. Further advantages of semiconductor detectors with respect to gas detectors can be listed as follows [14]

- high density of semiconductors, which allows to achieve large energy loss per traversed distance and allows to make the detectos thin,
- high mobility μ of charge carriers (in silicon μ of electrons is $\approx$ 1400 $\mathrm{cm^2 \cdot V^{-1} \cdot s^{-1}}$ and μ of holes is $\approx$ 450 $\mathrm{cm^2 \cdot V^{-1} \cdot s^{-1}}$ [15]),
- excellent mechanical rigidity,
- possibility to integrate sensitive volume and signal processing circuits [14].

In order to have better understanding of semiconductor detectors, let us briefly remind basics of the Band theory [16], which describes energy spectrum of electron levels in solids. Quantum mechanics predict, that discreet electron energy levels of isolated atoms evolve into energy bands once the atoms are placed close to each other on a crystalline lattice. In energy band, the electron levels are so close to each other that electrons can move from one to another level. Such transition between levels requires minimum energy, which can be obtained, for example, by thermal motion. The allowed energy bands are valence band and conduction band.

In different materials energy bands have different relative positions. There are three groups of materials according to the configuration of bands: insulators, conductors and semiconductors [16], see Fig. 1.1. Insulators have a width of the forbidden band larger than 2 eV. Conductors do not have the forbidden band. Semiconductors are characterized by a band structure where the valence band and the conduction band are separated by a narrow forbidden band. In semiconductors, the width of the forbidden band is less than 2 eV [13], so even a small thermal excitations can provide sufficient energy to electrons to overcome the band gap. For example, the forbidden band of silicon with temperature 273 K is about 1.1 eV [13]. Let us also point out that silicon is an indirect semiconductor which means that electron states in the conductive and in the valence band have different momenta [14].

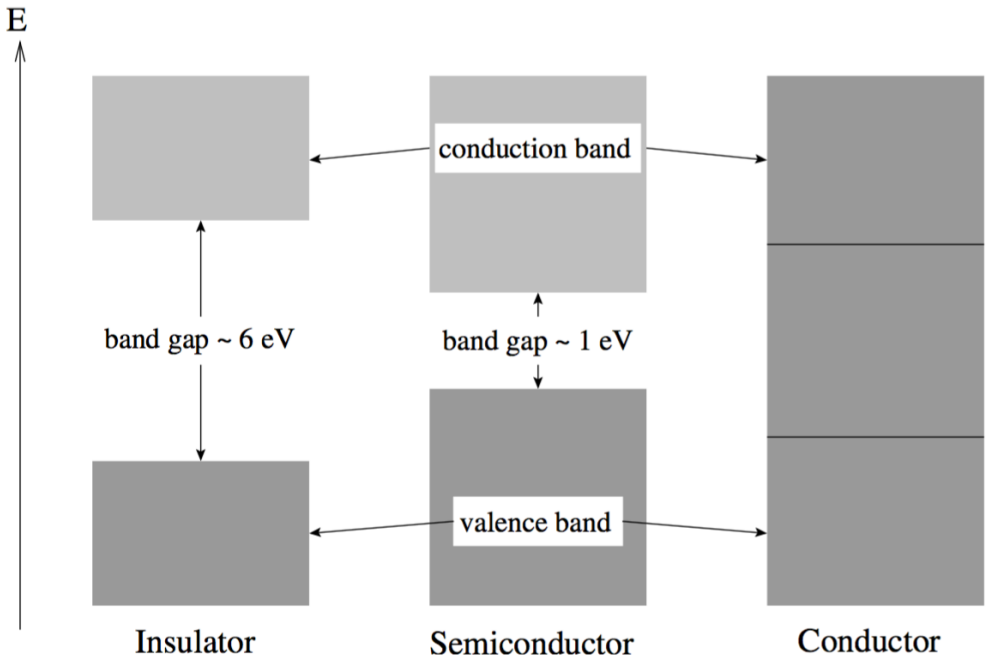

Figure 1.1: Energy band diagrams for insulator, semiconductor and conductor, taken from [16].

Excitation of an electron in the valence band of a semiconductor leads to creation of a hole in the valence band and a free electron in the conductive band. The combination of these charges is called $electron-hole\ pair$. If an electric field is applied to the semiconductor, free electrons and holes start to move in opposite directions. The probability that a free electron will have energy E is given by the Fermi function $f(E)$ [16]:

$$f(E) = \frac{1}{1 + e^{(E-E_F)/kT}}, \tag{1.1}$$

where k is the Boltzmann constant, T is the temperature, E_F is the Fermi level, which is the energy level which electrons occupy with the 50% probability. By integrating Fermi function and carrier concentration we get the density of free electrons n:

$$n = 2\left(\frac{2\pi m_n kT}{h^2}\right)^{\frac{3}{2}} e^{-\frac{E_C - E_F}{kT}} = N_C e^{-\frac{E_C - E_F}{kT}}. \tag{1.2}$$

Similarly for the density p of free holes we obtain:

$$p = 2\left(\frac{2\pi m_p kT}{h^2}\right)^{\frac{3}{2}} e^{-\frac{E_F - E_V}{kT}} = N_V e^{-\frac{E_F - E_V}{kT}}. \tag{1.3}$$

Here m_n is effective electron mass, m_p is effective hole mass, h is Planck's constant, T is the absolute temperature, E_C is a conduction energy level, E_V is a valence energy level, E_F Fermi level, N_C and N_V are the effective densities of states in the conduction and valence bands.

In a pure semiconductor with no impurities, electron-hole pairs are produced by thermal excitation (without ionizing radiation), each excited electron leaves the hole behind, so the number of electrons in the conduction band and holes in the valence band is equal:

$$p = n = n_i, \tag{1.4}$$

where n_i is intrinsic concentration [14]. Such materials are called ideal semiconductors or *intrinsic* [16].

Ideal semiconductor, however, doesn't exist in nature. Crystal impurities and defects imply additional energy levels within the forbidden band, which change the conductive properties of material. The electron and hole densities then do not have to be in equilibrium. In general, any adding of impurity causes a change of conduction properties of material. Material with added impurities is called *extrinsic* semiconductor and the process, which leads to its creation, is called *doping*. The impurity that causes increase of the number of holes in semiconductor is called *acceptor* impurity and the impurity that increases the density of electrons is the *donor* impurity [16]. Generally, small density of impurities is needed for semiconductors used as a radiation detector. For example in silicon based semiconductors for each impurity atom there are $\approx 10^{10}$ atoms of Si. When density of majority carriers (in the case of n - type semiconductor carriers are electrons) increases, the density of minority carriers decreases [14]:

$$n \cdot p = n_i^2. \tag{1.5}$$

1.1 Effect of Impurities or Dopants

1.1.1 p-type semiconductors

If the impurity added in semiconductor has less valence electrons than the initial semiconductor elements, it will capture a valence electron from a neighboring atom and form less bonds than semiconductor atom does. This will also create extra holes in extrinsic semiconductor. Such materials are known as p-type semiconductors. These semiconductors have additional acceptor type energy levels near the valence band. For example, by adding boron in silicon, one will obtain acceptor level with energy $E_A = E_V + 0.045$ eV [14], where E_V is the valence band energy, see Fig. 1.2 left. Because 0.045 eV is a small energy, even thermal energy can overcome it, so that the impurity atom will be ionized. In Fig. 1.2, right the acceptor doping of silicon by boron is shown.

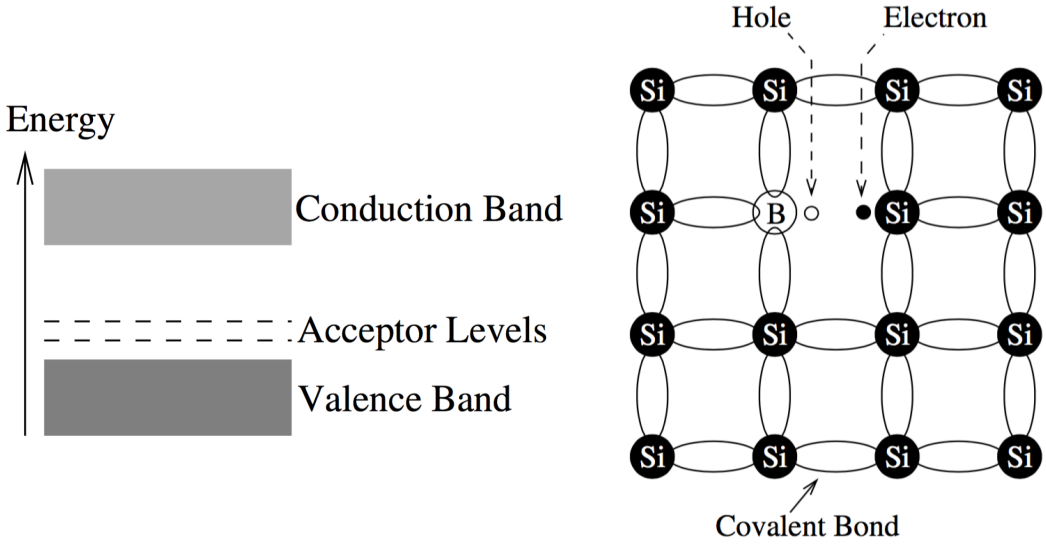

Figure 1.2: Left: energy band diagram with acceptor levels, [16]. Right: doping of Si lattice by boron. Since boron has one electron less, it can form only 3 covalent bonds with silicon atom. The fourth unfilled band behaves as a hole since it attracts free electrons. If this hole is filled by a neighboring electron, it will appear at the initial place of this electron. [16].

1.1.2 n-type semiconductors

If the impurity element has more valence electrons than the semiconductor atoms, the extra electrons are not able to make covalent bonds with semiconductor atoms, so they are free. Such a semiconductor material with a donor impurity is called an n-type semiconductor. Doping with donor impurity creates new donor type energy levels near to the conduction band. Similarly as in p-type semiconductors,

phosphorus in silicon makes donor level with energy $E_D = E_C - 0.054$ eV [14], where E_C is the conduction band energy, see Fig 1.3 left. These extra levels cause that the forbidden gap is effectively reduced, which improves the conduction properties of material. In Fig. 1.3 right the donor doping of silicon by phosphorus is shown.

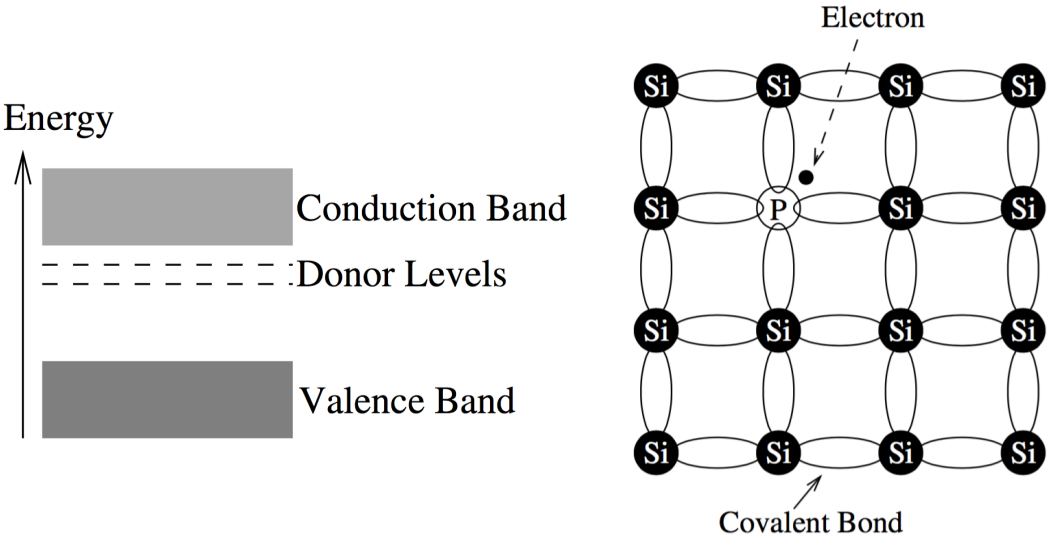

Figure 1.3: Left: energy band diagram with donor levels, [16]. Right: doping of Si lattice by a phosphorus atom. Since phosphorus atom has 5 available electrons for bonding, but since silicon has only 4 valence electrons, one extra electron from phosphorus outer shell becomes free, [16].

1.2 The pn - Junction

The basis of all semiconductor detectors is the so-called pn-junction, which is obtained by joining together n-type and p-type semiconductors. When a p- and n-type semiconductors are brought together, electrons will diffuse into the p region and holes into the n region to compensate the imbalance across the junction. As a result of diffusion and recombination process the concentration of negative charge will decrease at the border of the n region, which will become positive. Similarly at the border of the p region the concentration of holes will decrease, so this region will become negative. In this way, an electric field will be created, which counteracts the further diffusion, creating a depletion zone (region free of mobile carriers) with a potential between p- and n- region, the so-called built-in voltage V_{bi}, see Fig. 1.4:

$$V_{bi} = \frac{kT}{q} \ln \left(\frac{N_d N_a}{n_i^2} \right), \tag{1.6}$$

where N_d and N_a are donor and acceptor concentrations on the n and p sides, q is the unit charge [17]. The depletion zone is a sensitive zone in semiconductor

detectors, where the incident radiation creates electron hole pairs. Created charges flow with respect to electric field making a current and associated voltage drop, which can be measured. However the junction is too thin for effective radiation detection and the potential is also small. The width of depletion region can be regulated by applying external voltage. Applying positive potential to the p-region and negative to the n-region, the potential barrier reduces and the current across the junction increases. When the opposite polarity is applied (back bias), the potential barrier increases and the width of the depletion grows, this regime is used in detectors.

The width of the depletion zone w with applied external back bias V_{bb} is given by:

$$w = \sqrt{\frac{2\epsilon}{e}\frac{N_a + N_d}{N_a N_d}(V_{bi} - V_{bb})}, \tag{1.7}$$

where ϵ is the dielectric constant, e is elementary charge [17].

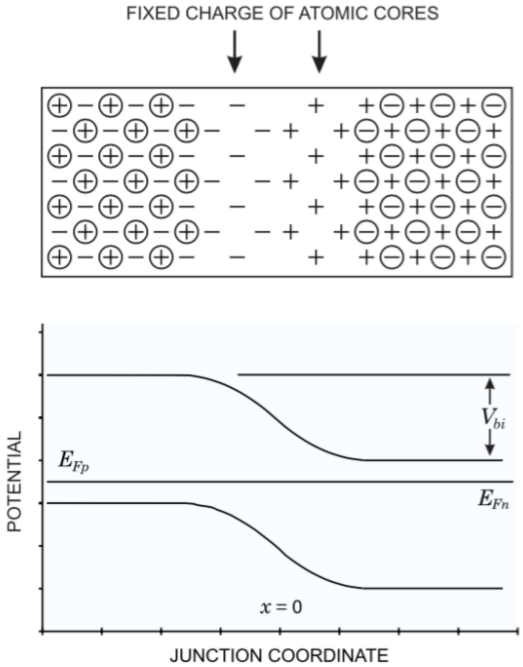

Figure 1.4: Diffusion of electrons and holes across the pn-junction forms a depletion zone with a built-in potential V_{bi} between the p- and n-regions, E_{F_n} and E_{F_p} are Fermi levels of n- and p-regions, [17].

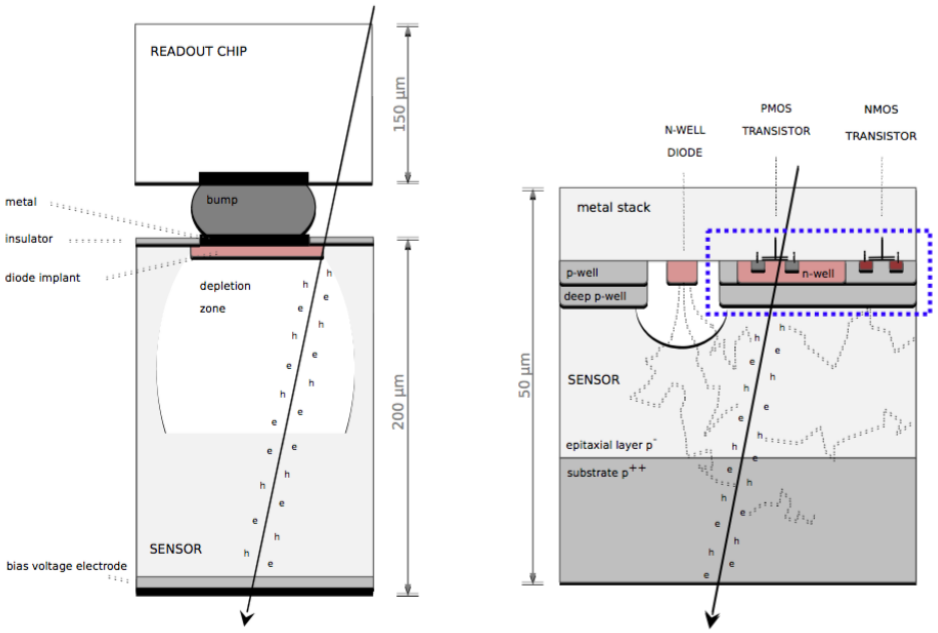

Figure 1.5: To the left: Hybrid pixel sensor, sensitive layer and front-end circuitry are separated by bump bond [18]. To the right: MAPS. The front-end circuitry is located in the blue marked area [18].

1.2.1 Position sensitive semiconductor detectors

The silicon detectors have different structures and configurations: strip detectors, hybrid pixel detectors, Charged Coupled Devices (CCD), Silicon Drift Detector (SDD), Monolithic Active Pixel Sensors (MAPS) and other [14].

The current ALICE ITS innermost layers consist of hybrid pixel detectors. In those detectors, the CMOS chip, which includes the front-end and the read-out logic, and the sensitive layer are separated by fine pitch bump-bonding. This allows to optimize both parts separately. Furthermore by applying larger bias voltages, one may obtain the full depletion with larger electric fields, which leads to faster charge collection and higher efficiency [18]. However, hybrid pixel detectors can not fulfill the requirement of the new ITS to reduce the material budget. Moreover, they are complicated to construct and relatively expensive.

Monolithic Active Pixel Sensors (MAPS) combine front-end circuitry and sensitive layer in one layer of silicon in comparison to hybrid pixel sensors, see Fig. 1.5, which allows to reduce material budget. However they were not used in tracking systems because of the limited radiation tolerance and slow readout. The TowerJazz 180 nm CMOS technology improved MAPS performance, so they were chosen for ALICE ITS upgrade, see chapter 2.2.

1.3 Signal generation is silicon sensors

Charged particles crossing material deposit part of their energy by means of scattering processes with the electrons of the medium. The mean energy loss per unit traversed length is described by the Bethe-Bloch formula [13]:

$$\left\langle -\frac{\mathrm{d}E}{\mathrm{d}x} \right\rangle_{\mathrm{ion}} = \frac{4\pi z^2 e^4}{m_e v^2} n[\ln \frac{2m_e v^2}{I_{\mathrm{ion}}(1-\beta^2)} - \beta^2 - \delta - U], \tag{1.8}$$

where z is the particle charge, v is the velocity of a particle, c is the speed of light in vacuum, $\beta = \frac{v}{c}$, n is the density of electrons in medium, I_{ion} - excitation energy of atom, δ - correction for material density and U is correction for binding energy of electrons on orbitals K, L and others. The energy loss depends on the path length of the particle in the material and is minimal for particles with $\beta\gamma \approx 3-4$ (Minimum Ionizing Particles).

The charge collection mechanism of pixel detectors is the following. Generated free charge carriers diffuse across the epitaxial layer, which is not fully depleted, until reaching the drift region of an n-well diode, where they are collected. The measured voltage drop V is given by the diode capacitance C and the collected charge Q:

$$\Delta V = \frac{Q}{C}. \tag{1.9}$$

If capacitance is small, then even a small collected charge is enough for high ΔV.

1.4 Radiation damage in semiconductors

The performance of semiconductor detector depends on its radiation hardness. Radiation can cause serious lattice damage, which can affect efficiency of charge collection inside of the semiconductor detector [17]. The overall damage depends on instantaneous and integrated doses. Radiation can affect the semiconductor by two basic mechanisms:

- **Displacement of material atoms**, which destroys lattice structure. This damage uses Non Ionizing Energy Loss (NIEL) scaling [17], which allows to compare the damages caused by different radiations. Such defects can be scattered or clustered around the particle trajectory. The isolated atomic displacements away from each other are called point defects. A cluster of atomic displacements close to each other is called a cluster defect. The primary knocked-on atom (PKA) moved by NIEL from initial sites can cause further damage, which is not a part of NIEL. In contrary to ionizing energy loss, NIEL is not proportional to absorbed energy, but it depends on type of radiation and particle energy. NIEL damage caused by an incident

particle with energy E is given by:

$$D(E) = \sum_i \sigma_i(E) \int_0^{E_{R,max}} f_i(E, E_R) P(E_R) \mathrm{d}E_R, \tag{1.10}$$

where $\sigma_i(E)$ is a cross section of the i-th interaction, $f_i(E, E_R)$ is a probability of generation of a PKA (Primary Knock-On Atom), E_R is a recoil energy and $P(E_R)$ is a fraction of energy that goes into the displacement of a silicon atom [19], $D(E)$ is calculated over all possible interactions. In Fig. 1.6 the dependence of NIEL damage function on energy of initial particle for different particles is shown. NIEL is used to be normalized to 1 MeV neutron equivalent [14]. For example protons of energy 30 MeV used in radiation hardness tests presented in this work have the $D(E)/95$ MeV·mb ≈ 2.

- **Ionization damage** basically affects the surface and insulating SiO_2 layers of the sensor. This damage is scaled by total ionizing dose (TID). Ionizing radiation creates electron-hole pairs in the oxide layer. Because electrons have high mobility in the oxide, they are collected by the nearest positively biased electrode. As holes have low mobility and move very slowly in the direction of the electric field, they may be captured by interface trap. This leads to the change of circuit operation. Ionization effects strongly depend on the absorbed energy and are independent of the type of radiation [17].

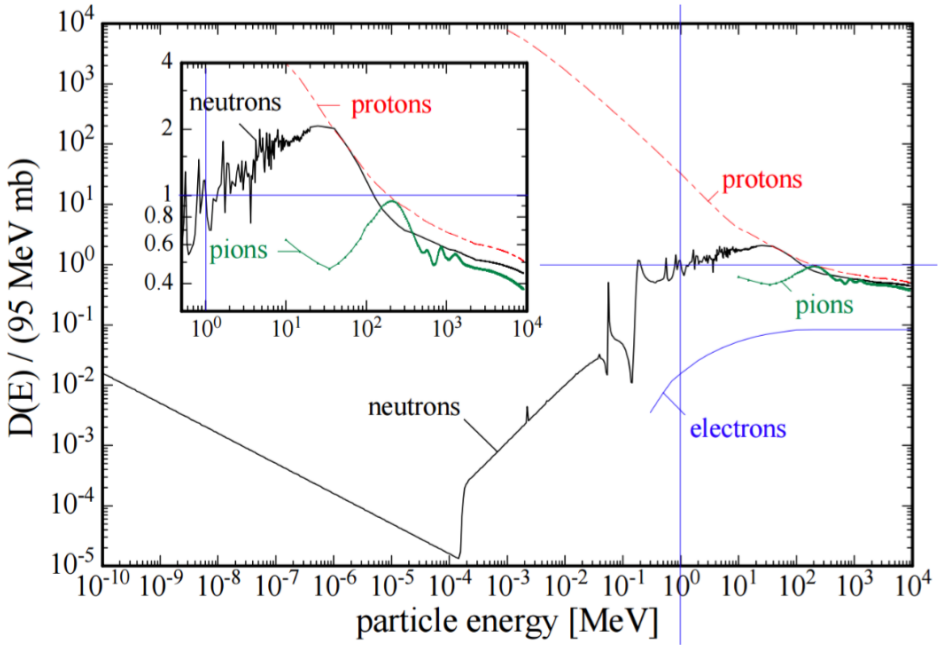

Figure 1.6: Damage function normalized to 95 MeV·mb for neutrons, electrons, protons and pions, which corresponds to NIEL 1 MeV n_{eq} [20].

1.4.1 Effects of radiation damages in semiconductor detectors

Properties of semiconductor detectors can change under the influence of radiation effects [16]. The most considerable are the following.

- **Increase of leakage current and charge trapping**. The radiation induced lattice defects make traps, which capture charge and liberate it very slowly. This charge contributes to the reverse bias current across depletion region. The increase of leakage current has unwanted consequences on detector performance, for example, increase in noise. Those traps may also function as recombination centers, which decrease detector efficiency. Moreover, some lattice defects can add extra energy levels to the band structure, making thermal excitations of electrons to the conductive band more probable, which also increases reverse bias. Fortunately the strong dependence on temperature can be exploited to compensate for the deterioration by decreasing the operating temperature.

- **Type Inversion**. Radiation may also affect impurity atoms, which may loose their function as acceptor or donor, becoming electrically inactive. Furthermore this can lead to the inversion of the material type, when an n-type material may change into a p-type and other way round after prolonged irradiation. This effect can be explained by the fact that radiation damage can change the effective dopant concentration in the material by increasing the charge carriers of the opposite sign. With increasing integrated radiation dose, the original dopant concentration may be overcome by the opposite charges.

  Radiation damage is to some extent repaired by the annealing process. This is a healing process, during which the radiation damage accumulated by detector decreases with time. Annealing process strongly depends on temperature, the defect concentration $N(t)$ can be parameterized as follows:

  $$N(t) = N_0 e^{-t/\tau}, \tag{1.11}$$

  where N_0 represents the initial defect concentration and τ is a function of the activation energy E_a and absolute temperature T:

  $$\tau = A e^{E_a/kT}, \tag{1.12}$$

  k is the Boltzmann's constant and A is determined experimentally [16].

Chapter 2

ALICE ITS upgrade

2.1 ITS upgrade

In this section, we will discuss the key features of the ITS upgrade, see Fig. 2.1. The main goals of the ITS upgrade are: to improve impact parameter resolution of reconstructed tracks, to improve tracking efficiency and p_T resolution at low p_T, to increase readout rate and to allow fast insertion and removal of the detector during the end of year technical stops. The comparison of current ITS performance and the upgraded ITS performance is shown in Fig. 2.2. Detailed discussion of the new ITS can be fount in [8], here we will highlight the the basic improvements of ITS:

- **Shifting the first detection layer closer to the beam line.** The reduction of the beam pipe diameter in the centre of the ALICE detector is one of the main points which will help to improve the impact parameter resolution. The current beam pipe with radius 29 mm will be replaced by a beryllium beam pipe having a radius of 17.2 mm. The wall thickness of the beam pipe is assumed to be 0.8 mm. The innermost detector layer can thus be moved closer to the interaction point from the current 39 mm to 23 mm.
- **Geometry and segmentation.** The baseline solution for the layout of the ITS upgrade is to replace six cylindrical layers of silicon pixel, drift and strip detectors with seven concentric cylindrical layers covering a radial extension from 22 mm to 430 mm with respect to the beam line. The upgraded ITS will cover the pseudo-rapidity range of $|\eta| < 1.22$ for 90% of the most luminous beam interaction region.
- **Reduction of material budget.** This will allow the tracking performance and momentum resolution to be significantly improved. The MAPS, which will be used will allow to reduce material budget per layer in comparison to the present ITS (50 μm in IB instead of 350 μm). The pixel density will be increased by a factor of ≈ 24. The pixel

size will be reduced from 50 μm $\times$ 425 μm to 29.24 μm $\times$ 26.88 μm. The area covered by MAPS will be 10 m^2. In total, there will be 24 000 sensors.

– **Readout time.** The present ITS has a maximum readout rate of 1 kHz. The new detector is designed to be able to read the data in a continuous readout or triggered mode up to the rate of each individual interaction up to a rate of 100 kHz for Pb–Pb collisions and 400 kHz for pp collisions.

– **Fast insertion removal.** The rapid accessibility to the detector for maintenance and repair interventions during the yearly LHC shutdowns will also be provided.

The characteristics listed above will enable the track position resolution at the primary vertex to be improved by a factor of 3 or larger. In the next section, we give more details about the pixel sensors that will be used in the new ITS.

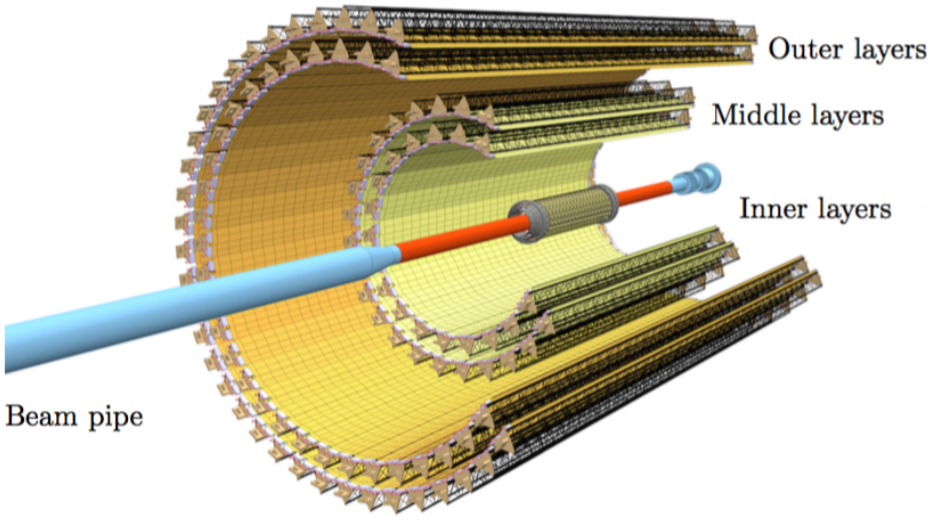

Figure 2.1: Layout of the upgraded ITS, taken from [8].

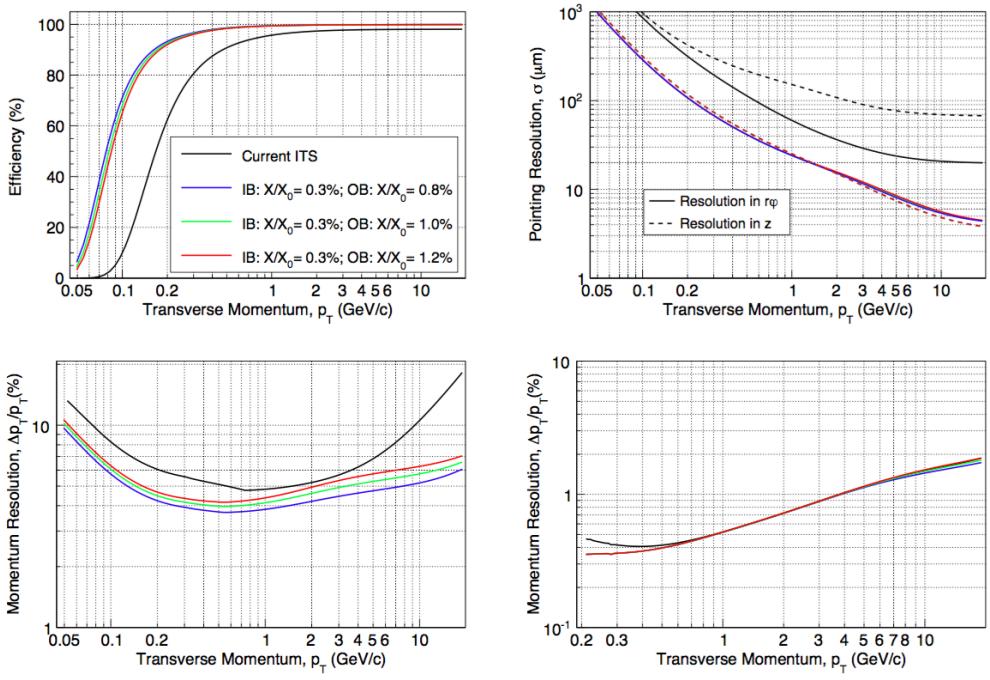

Figure 2.2: Top panels: Tracking efficiency (left) and pointing resolution (right) for charged pions vs. transverse momentum for the current ITS and different material budget options for the upgraded ITS. Bottom panels: transverse momentum (p_{T}) resolution for charged pions vs. p_{T} for the current ITS and different material budget options for the upgraded detector (the results for the ITS stand-alone and ITS+TPC combined tracking are shown on the left and on the right, respectively), taken from [1].

2.2 The ALPIDE chip

ALPIDE, which stands for ALICE PIxel DEtector [8], is a MAPS, see Section 1.2.1. The sensor has a size of 1.5 cm $\times$ 3 cm. It is divided into 512 rows and 1024 columns of pixels with a pitch of 29.24 μm $\times$ 26.88 μm. The current version of ALPIDE is a result of several year long process of research and development, during which several sensor prototypes were designed and tested [18, 22]. Table 2.1 shows the parameters of ALPIDE, it is seen that performance of the sensor satisfies all Inner and Outer Barrel requirements.

The ALPIDE uses the 180 nm CMOS technology of TowerJazz, see Fig. 2.3. This technology uses up to 6 metal layers which in combination with small size of pixel implements high density and low power digital circuits. TowerJazz also allows to use high-resistivity epitaxial layer and deep p-well, see Fig. 2.4. The thickness of sensitive layer is 18 – 30 μm. An additional deep p-well layer prevents the collection of charge carriers by the n-well of a

PMOS transistor that would compete with the n-well collection diode. This process feature, together with six metal layers, allows to use both PMOS and NMOS transistors for the implementation of complex CMOS circuits in the active sensor area. A moderate bias voltage can be applied to the substrate, increasing the volume of the drift region around the n-well collection diode and reducing its capacitance.

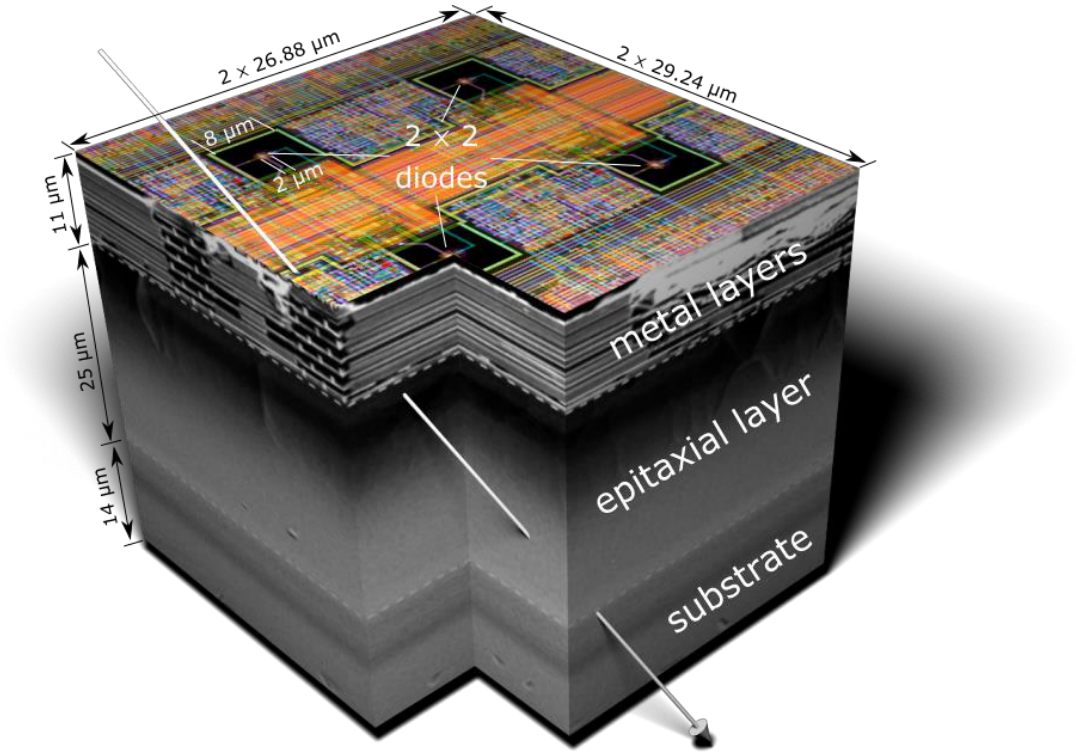

Figure 2.3: Sketch of a pixel of ALPIDE MAPS sensor with TowerJazz technology, taken from [1].

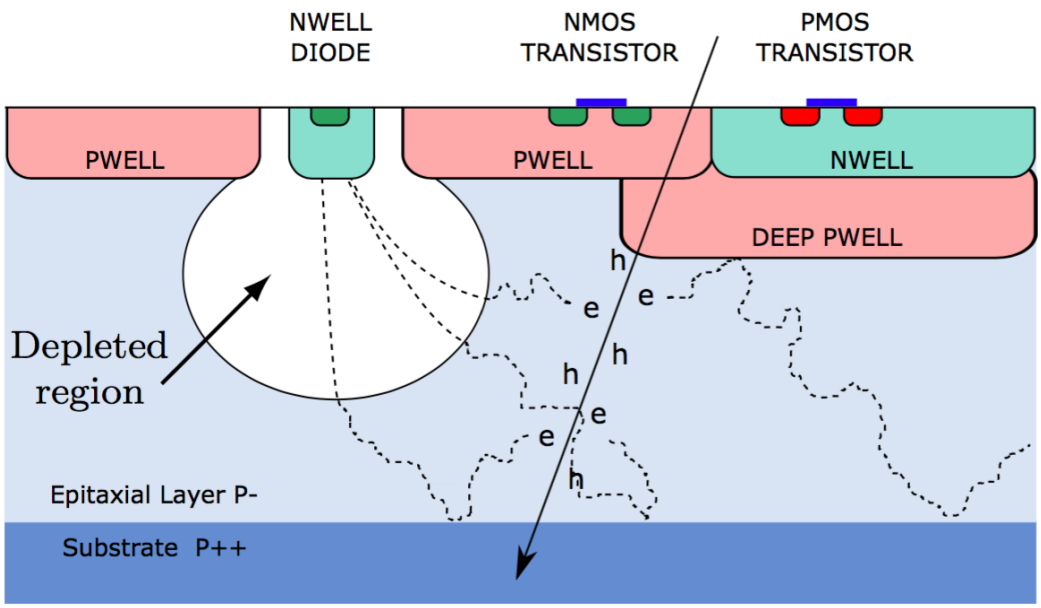

Figure 2.4: Schematic drawing of a pixel of ALPIDE MAPS sensor with TowerJazz technology, taken from [1].

	Inner Barrel	Outer Barrel	ALPIDE performance
Thickness [μm]	50	100	OK
Spatial resolution [μm]	5	10	~ 5
Chip dimension [mm]	15×30	15×30	OK
Power density [mW/cm^2]	< 300	< 100	<40
Event-time resolution [μs]	< 30	< 30	~ 2
Detection efficiency [%]	> 99	> 99	OK
Fake-hit rate [event^{-1}pixel^{-1}]	$< 10^{-6}$	$< 10^{-6}$	$< 10^{-10}$
NIEL radiation tolerance [MeV/n$_{eq}$/cm^2]	1.7×10^{13}	3×10^{10}	OK
TID radiation tolerance [krad]	2700	100	tested at 500

Table 2.1: IB and OB requirements, ALPIDE performance [22].

Each pixel of ALPIDE has an analog front-end circuit for signal amplification, hit discrimination and a 3 hit buffer. First, charge is collected on the collection diode or injected through the capacitance C_{inj}. The generated current causes a voltage drop on the PIX_IN node. After that the signal is amplified and discriminated with respect to the chosen threshold level. The binary signal is then sent to the in-pixel memory. The principle of charge amplification and discrimination can be understood from Fig. 2.7 where the

in-pixel analog front-end is shown. The transistor M1 acting as a source follower forces the source voltage to follow the M1 gate voltage. The voltage drop at the PIX_IN node produces current between capacitances C_{SOURCE} and C_{OUT_A} resulting in a voltage gain. If there is a hit, the voltage at OUT_A node increases so the current through the M_8 gate increases. If this current will be larger than I_{DB}, there will be the discriminated signal at the OUT_D node, which is propagated to the in-pixel memory. The both voltage V_{CASN} and current I_{THR} define the baseline value of OUT_A node, when $I_{M8} < I_{DB}$. The charge threshold is defined by the distance of the OUT_A baseline voltage and the point when $I_{M8} = I_{DB}$. Increasing I_{THR} leads to the increase of the charge threshold, while increasing V_{CASN} reduces the threshold. In other words, charge threshold is influenced by two parameters: V_{CASN} and I_{THR}.

All the analog signals required by the front-ends are generated by a set of on-chip 8 bit DACs, which are implemented in chip, see Fig. 2.5. All of the voltages are beginning with V (V_{CASN}, V_{CASN2}, V_{CASP}) and currents with I (I_{THR}, I_{DB}, etc.)

2.6.

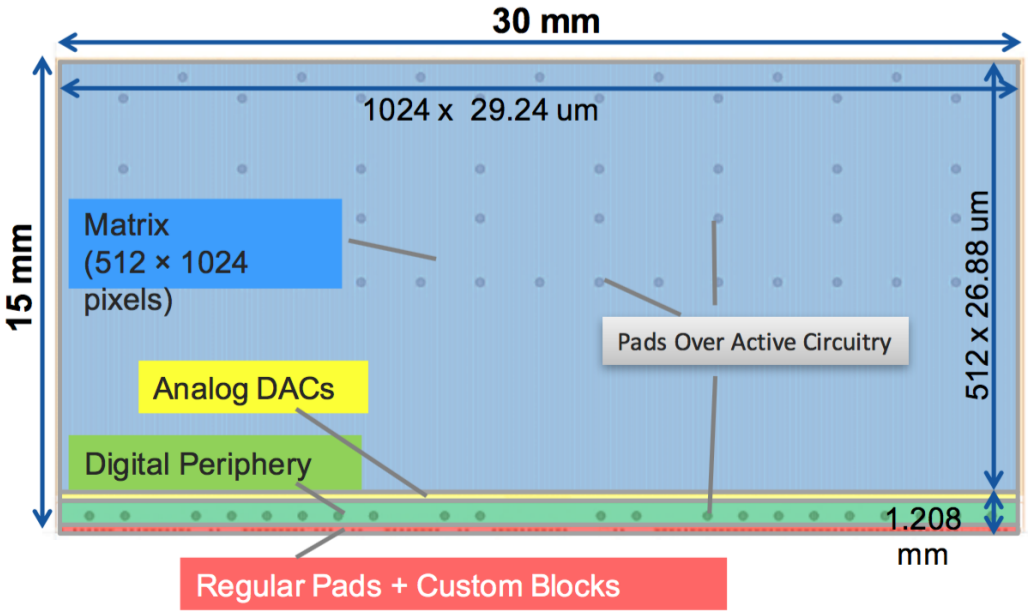

Figure 2.5: Scheme of the ALPIDE pixel with analog DACs in the bottom, taken from [21].

After the discrimination the signal goes to the address decoder AERD. The address encoding of the hit pixels is provided by Address-Encoder Reset-Decoder (AERD) logic. AERD is built as a tree structure. Each element of

the level represents 4 elements of underneath level, the lowest level is pixels level. The signal processing before the AERD logic is shown in Fig. 2.6.

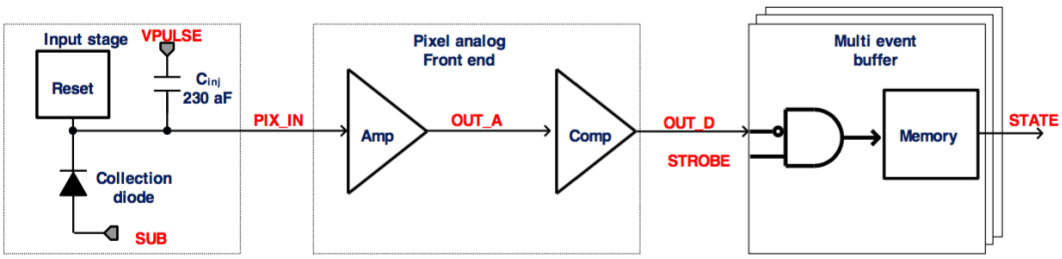

Figure 2.6: Scheme of the in-pixel signal processing, taken from [22].

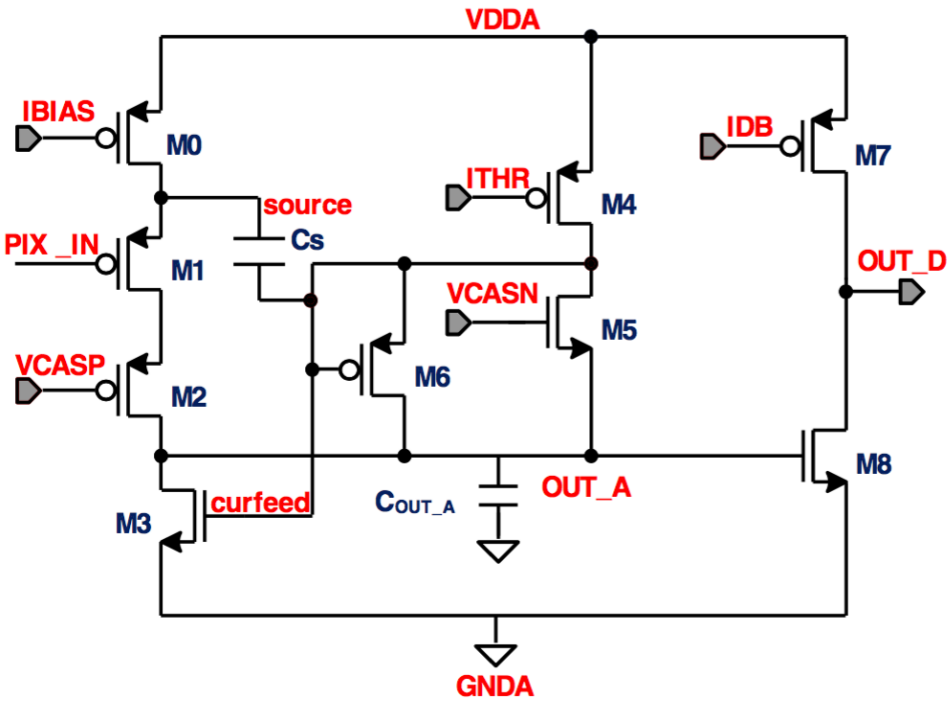

Figure 2.7: Analog frond-end schematic practical implementation, taken from [22].

Chapter 3

Experimental Setup for radiation hardness tests of ALPIDE

The main goal of this work is to test the radiation hardness of the ALPIDE chip. In this chapter, we will describe the experimental setup used for radiation hardness tests at the U-120M cyclotron.

3.1 Cyclotron U-120M

Cyclotron is a cyclic accelerator of charged non-relativistic heavy particles, protons and heavy nuclei, with a constant magnetic field [23]. A typical cyclotron scheme is shown in Fig. 3.1. Heavy charged particles are injected from an ion souce located at the center. The vacuum chamber is placed in a magnetic field which curves particle trajectories. Acceleration takes place between electrodes (dees), where the electrical field has a constant frequency. Dees have a shape of hollow cylinder. Original cyclotrons had two dees, however nowadays they may have more of dees.

Considering that vacuum chamber is placed in a homogeneous magnetic field B, we can calculate radius of particle trajectory R with mass m from the balance of the Lorentz force and centrifugal force.

$$R = \frac{mv}{QB}, \tag{3.1}$$

where v is velocity. The orbital frequency of a beam particle f is then

$$f = \frac{v}{2\pi R} = \frac{QB}{2\pi m}. \tag{3.2}$$

The acceleration of a particle between dees leads to increase of its kinetic energy E and the radius of the trajectory R. Kinetic energy of a particle at

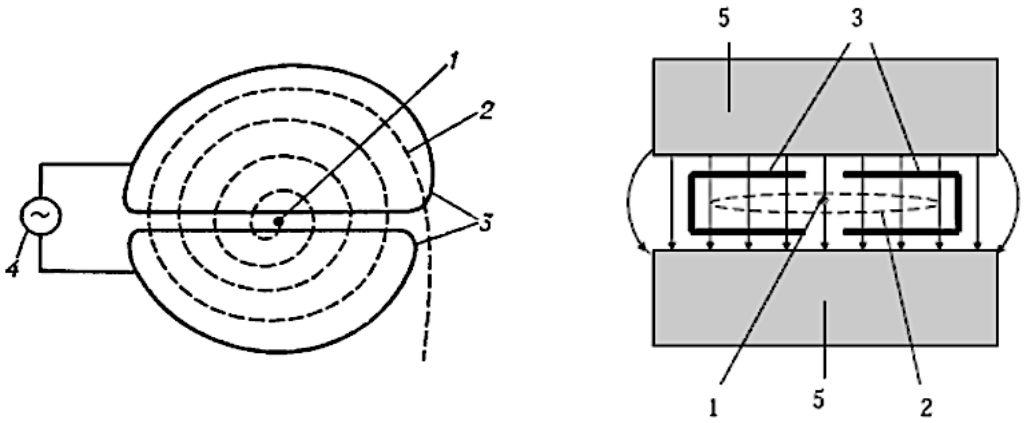

Figure 3.1: Scheme of a simple cyclotron: 1 is ion source of the particles, 2 is a trajectory of accelerated particles, 3 are dees, 4 is a generator of electric field, 5 is an electromagnet, taken from [23].

given radius can be calculated as

$$E = \frac{mv^2}{2} = \frac{Q^2B^2R^2}{2m}, \tag{3.3}$$

where velocity v is

$$v = \frac{QBR}{m}.$$

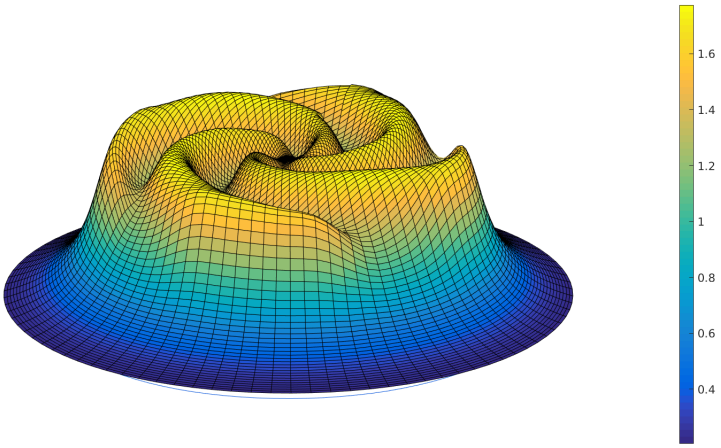

Figure 3.2: Distribution of magnetic field in the U-120M cyclotron in the horizontal plane going though the center of the vacuum chamber. The z axis shows the intensity of the field in Tesla [24].

Only the particles that pass between dees in a narrow time interval when the voltage between them is the highest fulfil the condition for subsequent

acceleration. The probability of successful particle acceleration decreases with increasing phase difference.

Homogeneous magnetic field however doesn't guarantee the focusation of the beam in cyclotron [25]. Therefore modern cyclotrons use a magnetic field which changes with azimuth [25]. In Fig. 3.2, the configuration of magnetic field used in the cyclotron U-120M is shown. Such field can compensate relativistic increase of particle mass, which guarantees the condition of isochronity [26].

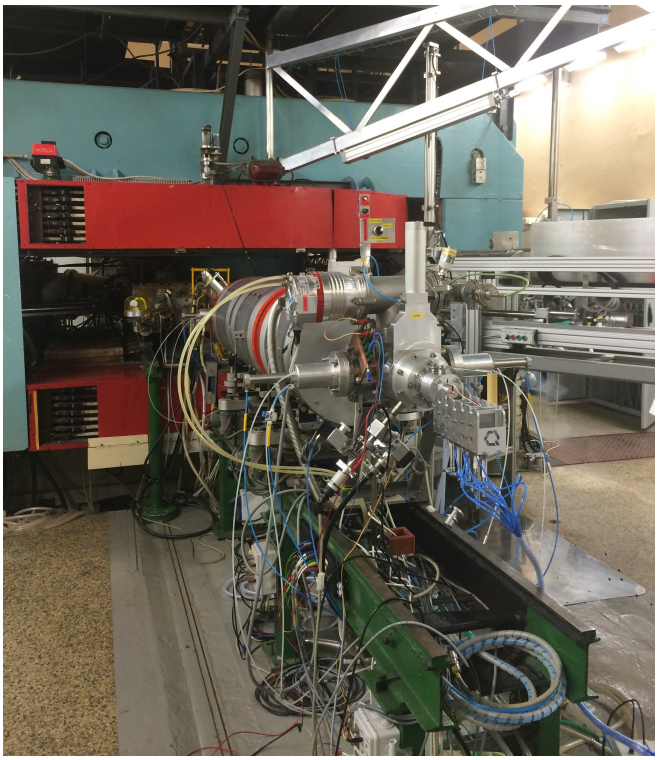

Figure 3.3: Cyclotron U-120M in the Nuclear Physics Institute of the Czech Academy of Sciences in Řež. Beam trace ensuring output of protons and deuterons from negative regime. The negative mode beam line that sticks from the cyclotron is terminated by the energy degrader.

To irradiate the ALPIDE chips, we used the isochronous cyclotron U-120M, which is located in the Nuclear Physics Institute of the Czech Academy of Sciences in Řež [27], see Fig. 3.3. This cyclotron has only one dee electrode, the function of the second dee takes the grounded vacuum chamber wall. The cyclotron is able to accelerate positive ions H^+, D^+, $^3He^{+2}$ and α and negative ions H^-, D^-. In Tab. 3.1 the parameters of the beam, that can be provided by the cyclotron, are shown. Positive and negative particles are accelerated in two different modes. Each mode has different extraction mechanism. The positive regime is used for acceleration of positive ions. It uses a magnetic kicker in combination with a system of electrostatic

deflectors, see Fig 3.4 left. The negative regime accelerates negative ions, the polarity of the extrinsic magnetic field is reversed in this mode, so particles are accelerated in the same direction as in the positive mode. By passing through a 1 μm thick carbon foil, negative ions lose valence electrons and become positive. The final positively charged beam is then bent out of the vacuum chamber by the Lorentz force and is directed to a short beam line, see Fig 3.4 right. The beam line is equipped with 3 quadrupole magnets, which focus the beam and it is terminated with a 55 μm thick aluminum exit window. When compared to the positive mode, the negative mode has higher efficiency of beam extraction, because the positive mode has large beam losses on the electrostatic deflectors. On the other hand, the negative regime has greater uncertainty in the extracted energy of the final beam (about 0.25 MeV [29]). In our tests, the negative mode was used.

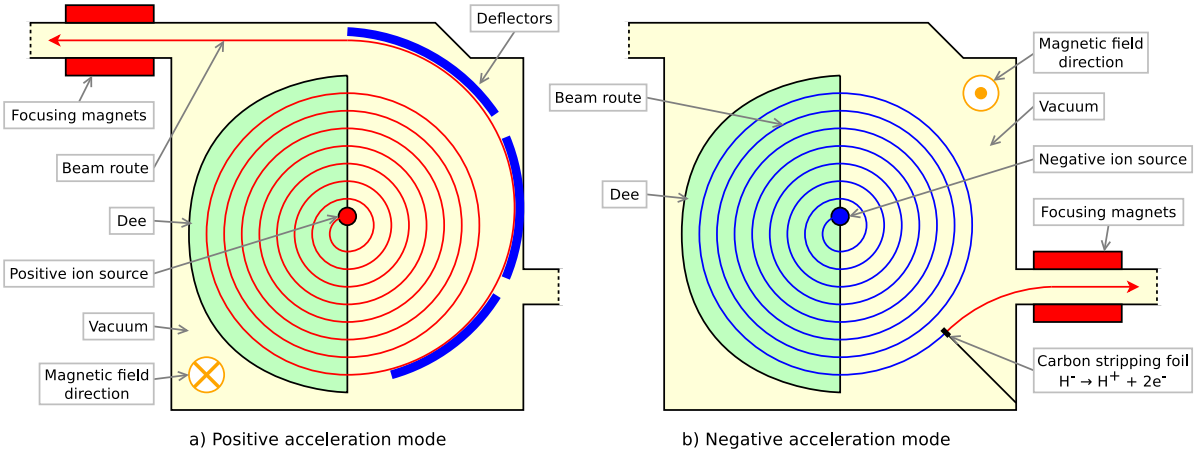

Figure 3.4: Acceleration modes of the cyclotron U-120M [28].

Ion	E[MeV]	$I_{\max}[\mu A]$
H^+	6–25	5
H^-	6–37	50–30
D^+	12–20	5
D^-	11–20	35–20
$^3He^{+2}$	18–52	2
α	24–38	5

Table 3.1: Kinetic energies and currents of accelerated particles in the cyclotron U-120M that can be achieved, taken from [26].

The time structure of the beam is shown in Fig. 3.5. The cyclotron works in the radio-frequency (RF) region 10–25 MHz [26]. The RF system is not operated in continious wave regime [29]. The RF accelerating system is protected against discharges by modulating the RF frequency with a 150 MHz

signal. This corresponds to a duty cycle period of 6.67 ms. The maximum allowed duty cycle (filling) can be changed in a range 4–65% of period, it depends on the generator frequency and on the number of particles in the acceleration chamber. The maximal allowed duty cycle for 35 MeV is 20%. In the experiment, we operate with lower duty cycles (5%) to reduce the proton beam intensity.

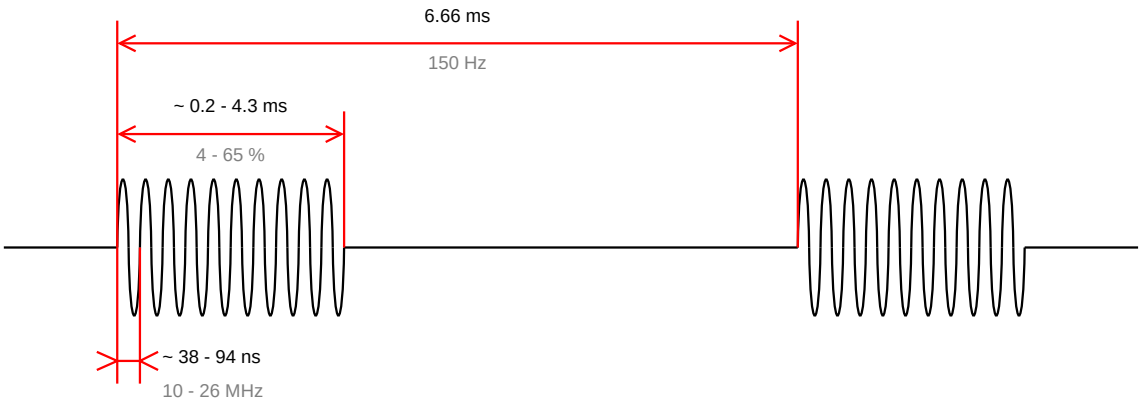

Figure 3.5: Time structure of the acceleration RF electrical field in the U-120M cyclotron. Filling can be varied between 4–65%, this corresponds to 0.2 – 4.3 ms long cycles when the cyclotron accelerates particles. This time is divided by RF to 38–94 ns long RF buckets, taken from [28].

3.2 Ionization chamber PTW 30010 Freiburg

The proton flux from the cyclotron is measured by an ionization chamber. In our measurement the ionization chamber PTW 30010 Freiburg was used [31]. This chamber has coaxial cylindrical geometry of aluminum anode and graphitic cathode. The surface of the cathode has a protective layer of Polymethylmethacrylate (PMMA). The chamber is filled with air which has atmospheric pressure. The average energy needed for electron-ion pair creation is thus 34 eV [32]. The sensitive volume of this chamber is 0.6 cm^3. The nominal working voltage is 400 V. The time of charge collection is 0.14 ms [31]. The ionization chamber PTW 30010 Freiburg and its scheme is shown in Fig. 3.6. Ionization current from the chamber is measured by the microprocessor-controlled universal dosimeter PTW - UNIDOS E [33], which is used also to set the working voltage in the chamber.

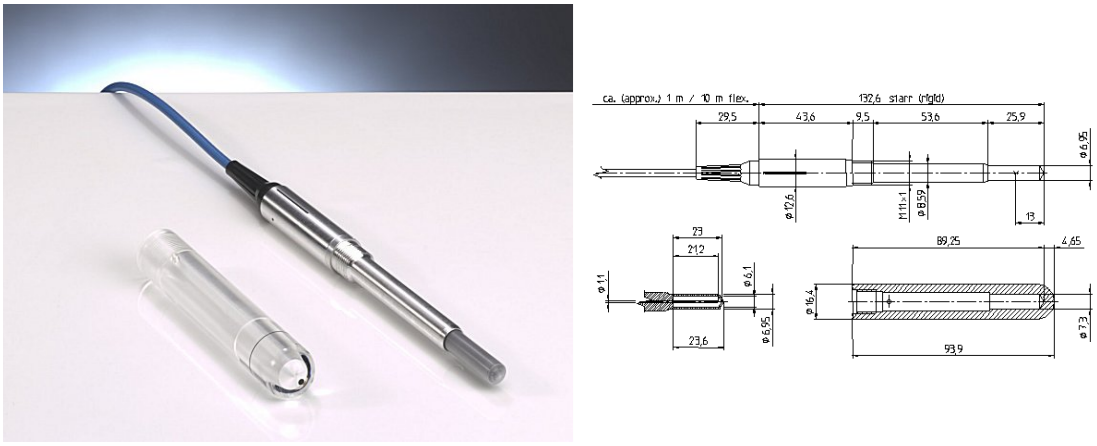

Figure 3.6: Left: photo of the ionization chamber PTW 30010 Freiburg, taken from [31], Right: the layout of ionization chamber PTW 30010 Freiburg. All dimensions are in millimeters. Thickness of the PMMA layer is 0.335 mm and of the graphitic cathode is 0.09 mm. The diameter of the aluminum anode is 1.1 mm, taken from [31].

3.3 Setup for irradiation tests at the U-120M cyclotron

The experimental setup for irradiation is shown in Fig 3.7. The beam line is terminated with a pneumatically controlled energy degrader unit, see Fig 3.8. This unit allows either to stop the beam or to change the beam profile and energy by insertion of aluminum plates of different thickness into the beam. The first plate is 8 mm thick and serves as a beam stop. The second plate is 0.56 mm thick and is used during ALPIDE irradiations to make the beam profile wider.

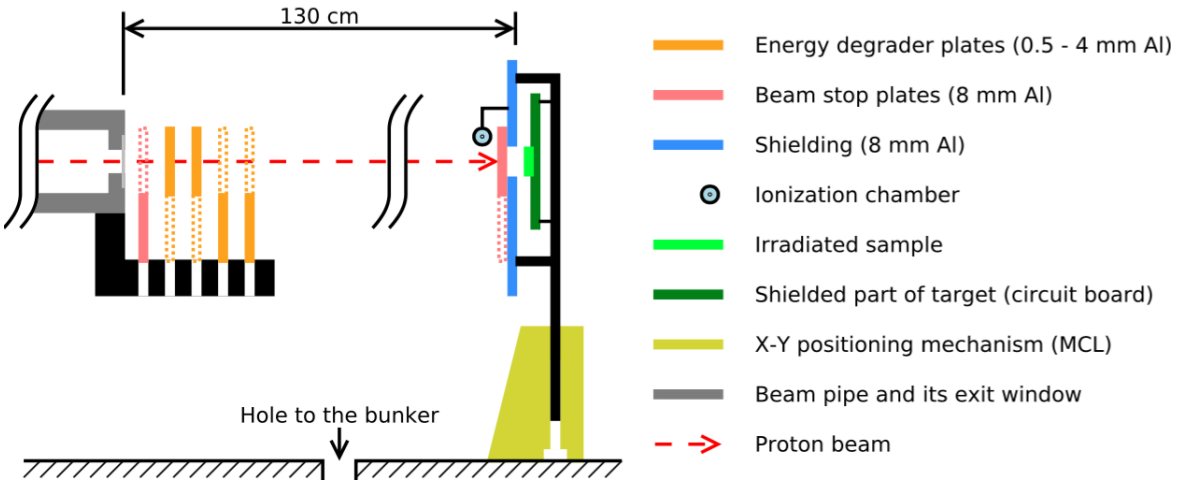

Figure 3.7: Illustration of the beam route from the beamline exit window to the irradiated sample through absorber plates. The sample, beam stop plate and ionization chamber are mounted on remotely controlled stage that allows to move the setup in the plane perpendicular to the beam..

Figure 3.8: Photo of degrader plates system behind the beam pipe exit window, in our experiment only one plate was used.

The irradiated sample (ALPIDE) is placed 130 cm away from the beamline exit window at the remotely movable stage together with the ionization chamber and an additional beam stop plate, see Fig 3.10 and Fig 3.9. The movable stage can move independently along X and Y axes with a step of

mm. The movable stage is controlled from a PC placed in the cyclotron control room, see Fig 3.10.

The relative position of irradiated sample and ionization chamber is fixed and is measured with the precision of 1 mm before each irradiation using laser tracker. The laser beam from the tracker shows an approximate position of the beam spot at the setup. Then we navigate the movable stage to the position in which the ionization chamber is in the laser spot and we pencil the corresponding coordinates. After that the stage is moved such that the center of the ALPIDE chip gets to the laser spot. The relative position of the ALPIDE and the ionization chamber is given by the difference of these two positions. The ionization chamber is used for on-line flux monitoring during the irradiation and for beam transverse profile scanning before the sample irradiation. The beam stop plate between the ionization chamber and the sample serves to prevent sample from being irradiated during the beam profile scanning.

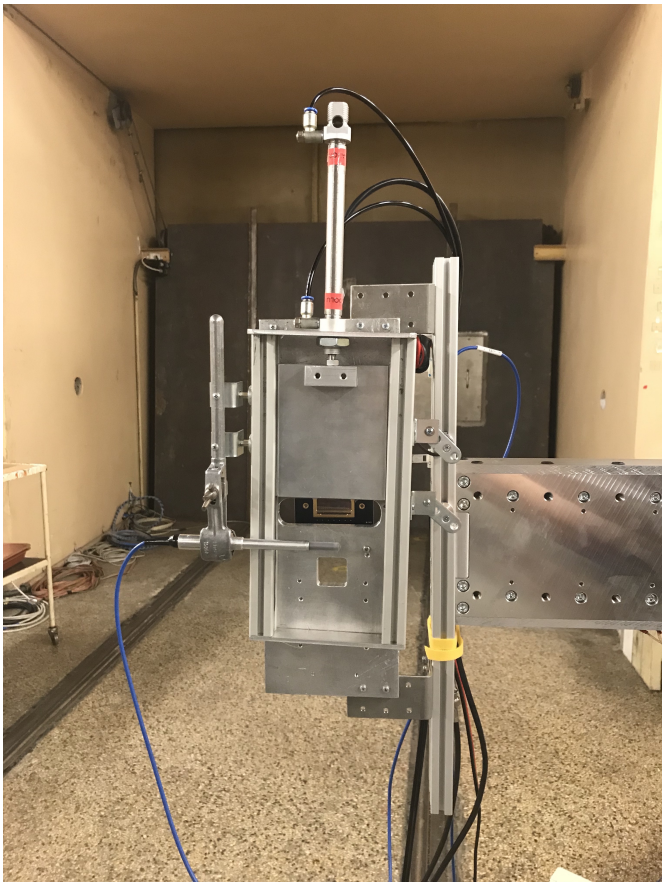

Figure 3.9: Photo of the frame with the ionization chamber, beam stop plate and the ALPIDE chip, all placed on the arm of the movable stage. The relative position of ALPIDE and the ionization chamber is fixed, the beam stop plate covers the chip during the beam profile scanning.

The scheme of cable network between devices is shown in Fig 3.10. The PC operating the ALPIDE chip, the energy degrader and the voltage source for ALPIDE is placed in the bunker. For its operating, the PC in the control room is used. Another PC is used for beam monitoring and movable stage regulating.

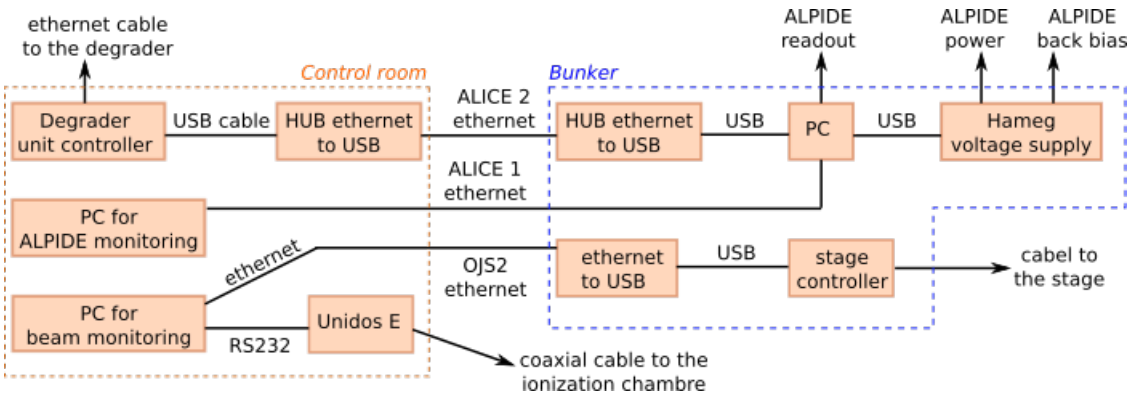

Figure 3.10: The logical connection of all basic devices for sample positioning and proton flux measurement used during the irradiation tests. The electronics for ALPIDE operation and stage controller are placed in the bunker under the cyclotron hall. The Ethernet cables are used to transfer signals over the long distance (≈40 m) between the control room and the bunker.

3.4 The irradiation process

The experiment at the cyclotron is made in the following way. First, position calibration of the movable stage is done. Then the ALPIDE is shielded with the second beam stop mounted on the movable stage and the beam profile along the horizontal and vertical axes is measured. The profiles are scanned stepwise in the traverse plane to the beam by moving the entire setup which is mounted on the stage perpendicular to the direction of the beam. The scan of the ionization chamber current takes about 1 minute for each axis.

After each scan the measured beam profiles are parametrized by the 1 dimensional Gaussian function, which gives the coordinates of the beam center with respect to the stage and the widths of the beam along the horizontal and vertical axes, see Fig 3.11.

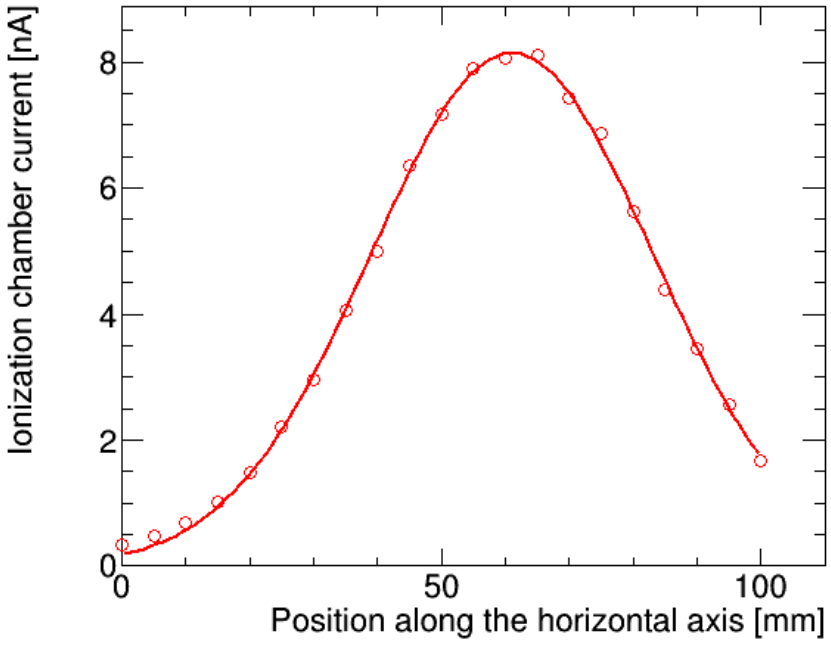

Figure 3.11: The transverse beam profile along the horizontal axis parametrized by a 1 dimensional Gaussian function in case of using one 0.56 mm thick aluminum energy degrader plate, σ is $\approx$ 2 cm.

From the fit, we can determine the coordinates of the center of the beam with an accuracy of 1 mm and the transverse width of the beam. Knowing the relative vertical distance between the center of ALPIDE and the center of the ionization chamber, we can determine the coordinates of the ALPIDE center.

In the next step, the second beam stop still covers the ALPIDE chip and the ionization chamber is placed at the beam center and the intensity of the beam is measured. After moving the stage to the position when the ALPIDE would be in the beam center, the current in the ionization chamber declines and is corrected by a factor determined from the Gaussian beam profile. During the irradiation we monitor ionization chamber current and use it to calculate instantaneous proton flux P with 10% accuracy [36, 37]:

$$P = I \cdot k, \tag{3.4}$$

where I is current in the ionization chamber and k is a known calibration parameter [36, 37]. Fluence F can be calculated by integrating the flux P:

$$F = \int_{t_0}^{t_0+t_{irr}} P \mathrm{d}t, \tag{3.5}$$

where t_0 is a time of the beginning of irradiation and t_{irr} is a period of irradiation. Finally, the total ionizing dose D is estimated by the formula

[38]:

$$D[\text{krad}] = 1.602 \times 10^{-8} \times \text{LET}[\text{MeV} \cdot \text{cm}^2 \cdot \text{mg}^{-1}] \times F[\text{cm}^{-2}], \qquad (3.6)$$

where LET is the stopping power (in our case in silicon). The formula is derived in Appendix A. The value of LET is taken from Stopping and Range of Ions in Matter (SRIM) simulation, the dependence of LET on energy of protons is shown in Fig. 3.12.

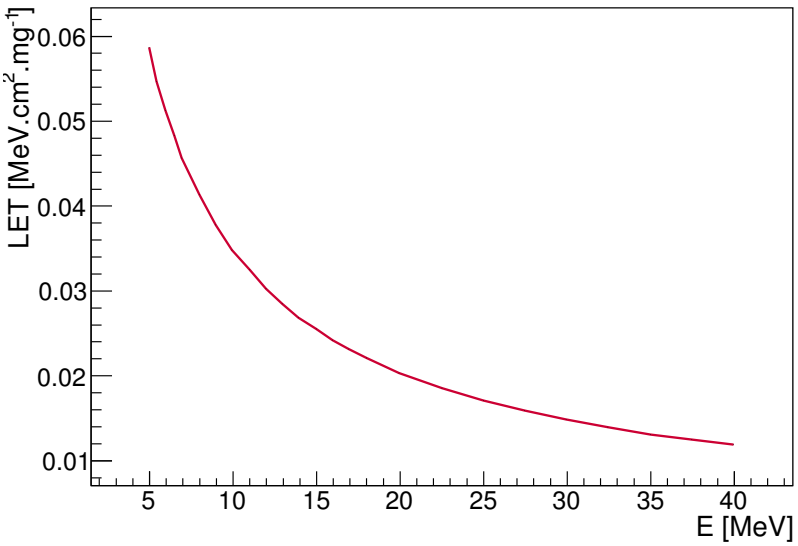

Figure 3.12: The dependence of stopping power of protons in silicon on energy of protons [35].

It is important to note that the irradiation of the chip is not continuous. The irradiations are interrupted by measurement of the activation function (the so-called threshold scan) and the DAC scan. The goal of the DAC scan is to test the response of the voltage and current sources which are implemented on the chip. While performing these scans the ionization chamber and the tested ALPIDE chip are covered by the first beam stop plate and aren't irradiated. Then the chip is uncovered again and analog and digital currents are monitored. After that the whole cycle is repeated. The measurement stops when the value of analog current reaches the half of initial value. This prevents that the chip gets destroyed. The default DAC settings are shown in Tab.3.2. Since November 2017, VCASN was made lower at 90 and VCASN2 at 102 to increase the threshold. During the irradiation the sensors are supplied with a voltage of 5 V and a moderate substrate reverse bias of -3 V. Due to the fact that the chips are sensitive to the light, all measurements are made in the darkness. Tests are performed at room temperature.

	Default settings	Settings from 11.2017
V_{CASN}	105	90
V_{CASN2}	117	102
V_{RESETP}	117	117
V_{RESETD}	147	147
V_{CLIP}	60	60
I_{THR}	51	51
I_{DB}	64	64
I_{RESET}	100	100

Table 3.2: Default DAC parameters and parameters set from November 2017.

Chapter 4

Analysis of radiation hardness tests at the U-120M cyclotron

In real conditions at the LHC, the ALPIDE sensors placed in the innermost layer of ITS IB will get the integrated ionization dose of 270 krad (integral over the RUN3). The expected average dose rate will be very small and it is supposed that annealing of radiation damage will have positive influence on detector functionality.

The detector proposal expects that the chip should survive the integrated dose that is ten times higher. To reach 2700 krad with the same dose rate as expected at the LHC would take several years of irradiation. This however cannot be done at the U-120M cyclotron due to economical and time reasons. Therefore the aim was to get reasonably close to the real conditions at the LHC and to divide the accumulated dose to the longer time period.

Radiation hardness of ALPIDE was tested in the series of measurements made at the cyclotron U-120M from September of 2016. Chips are irradiated by 30 MeV proton flux and typically gain a dose of 100 krad during one session. After the irradiation, the chips are left at rest at the room temperature. During this period chips anneal and their state is monitored.

Tests were made for two chips: A4W7G7R38 and A4W7G7R41. Those chips present the final design of ALPIDE. The thickness of the epitaxial layer is 25 μm.

I analyzed log files from irradiations and in Tab. 4.1 and Tab.4.2 I present doses and fluence accumulated during irradiations from September 2016 to July 2018, dose rates and average fluxes. Those parameters were obtained based on of current measured by the ionization chamber.

I used the log files also to draw the time evolution of dose and fluence during different irradiation campaigns, see Fig. 4.1, 4.2. As can be seen, the dependences are gradational. In the periods where the dependence is flat, the beam was blocked and the measurements of DAC characteristics and activation function were made. From Fig. 4.1, 4.2 it is seen that

the chip A4W7G7R38 was irradiated initially much faster than the chip A4W7G7R41. This was done in order to study whether the radiation damage depends also on the ionization dose rate. In the first irradiation the average dose rate for A4W7G7R38 was about 60 rad·s^{-1} while for A4W7G7R41 it was about 18 rad·s^{-1}. Let us point out, that the requited 2.7 Mrad was achieved by the chip A4W7G7R41 only in July 2018. The irradiation of chip A4W7G7R38 is in progress. Comparing the values of accumulated doses for both chips in Tab. 4.1 and Tab.4.2 it is seen that on average the chip A4W7G7R38 abided lower radiation load than the chip A4W7G7R41. This difference in radiation hardness is expected to be a consequence of the difference in dose rate during the first irradiation.

Date	Dose [krad]	Accumulated dose [krad]	Fluence [10^{10}·cm^{-2}]	Accumulated fluence [10^{10}·cm^{-2}]	Dose rate [rad.s^{-1}]	Average flux [10^{8}·cm^{-2}·s^{-1}]
9.2016	341	341	145	145	59.9	2.6
10.2016	122	463	52	197	64.7	2.8
12.2016	122	585	52	249	38.6	1.6
1.2017	89	675	38	287	49.1	2.1
3.2017	78	752	33	320	37.9	1.6
4.2017	90	842	39	358	18.8	0.8
5.2017	86	929	37	395	17.5	0.7
6.2017	96	1024	41	435	40.9	1.7
7.2017	87	1111	37	472	34.2	1.5
8.2017	94	1204	40	512	32.9	1.4
9.2017	86	1290	36	548	32.9	1.4
10.2017	87	1377	37	585	24.6	1.1
11.2017	84	1461	36	621	30.7	1.3
1.2018	108	1569	46	667	31.8	1.4
2.2018	111	1680	47	714	34.9	1.5
3.2018	110	1791	47	761	32.6	1.4
4.2018	95	1886	40	801	31.5	1.4
5.2018	114	2000	49	850	38.8	1.7
6.2018	100	2100	43	893	36.3	1.6
7.2018	24	2124	10	903	22.3	1.0

Table 4.1: Summary of irradiations for the chip A4W7G7R38.

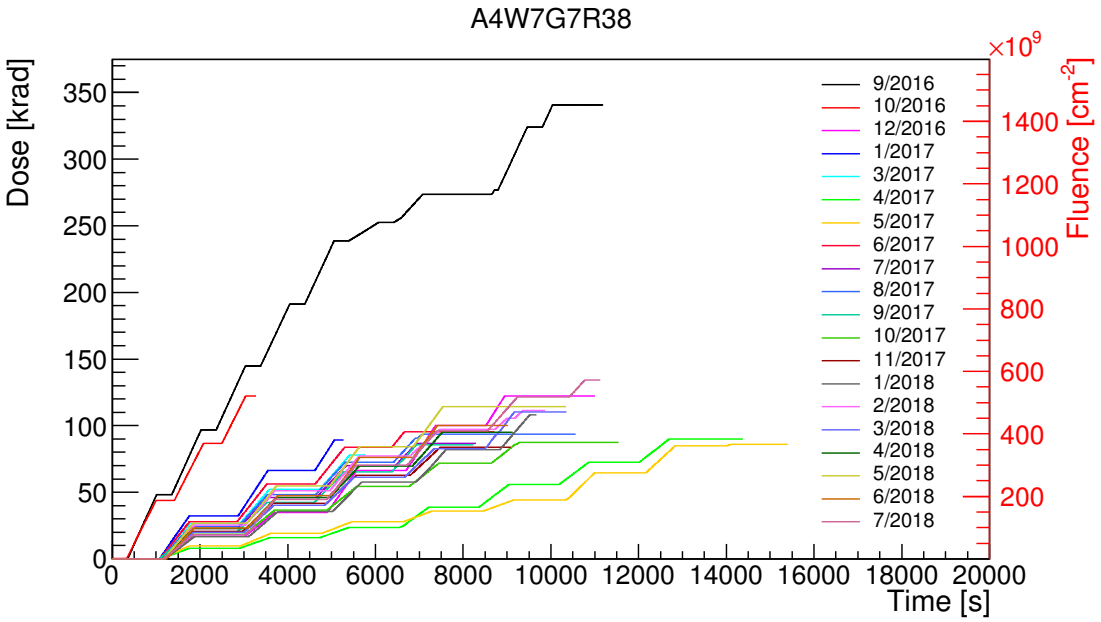

Figure 4.1: Total ionization dose and accumulated fluence for different irradiation campaigns for the chip A4W7G7R38.

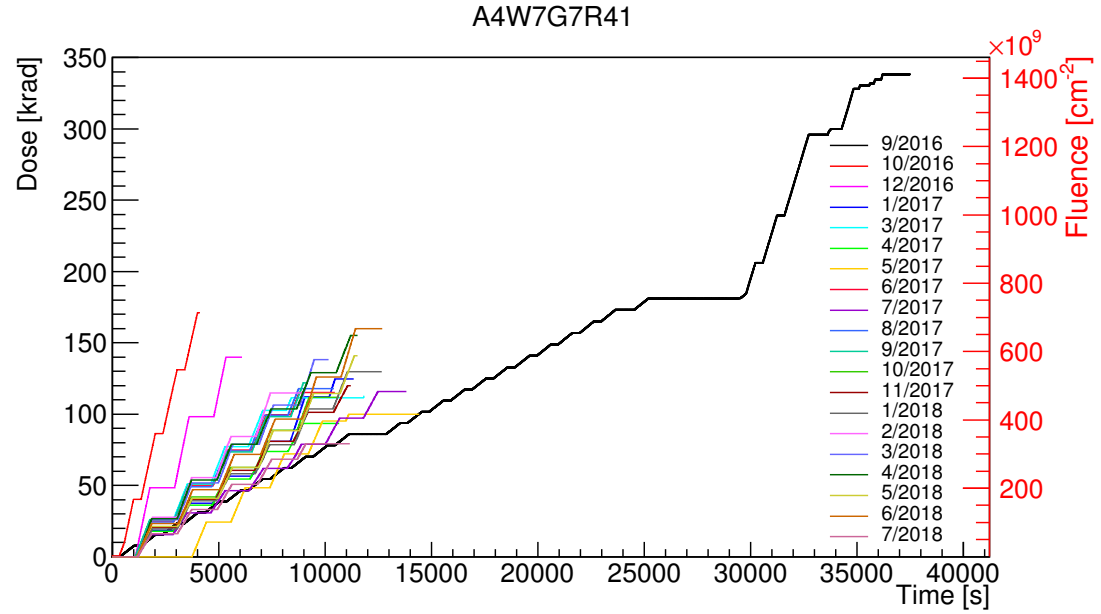

Figure 4.2: Total ionization dose and accumulated fluence for different irradiation campaigns for the chip A4W7G7R41.

Date	Dose [krad]	Accumulated dose [krad]	Fluence [10^{10}·cm^{-2}]	Accumulated fluence [10^{10}·cm^{-2}]	Dose rate [rad.s^{-1}]	Average flux [10^{8}·cm^{-2}·s^{-1}]
9.2016	338	338	144	144	17.8	0.8
10.2016	171	509	73	217	65.3	2.8
12.2016	140	649	60	276	72.1	3.1
1.2017	125	774	53	329	30.9	1.3
3.2017	113	886	48	377	37.5	1.6
4.2017	94	980	40	416	27.4	1.2
5.2017	100	1080	43	459	34.8	1.5
6.2017	115	1195	49	508	36.5	1.6
7.2017	116	1311	49	557	24.2	1.0
8.2017	118	1429	50	607	36.2	1.5
9.2017	122	1551	52	659	37.0	1.6
10.2017	112	1663	48	707	33.8	1.4
11.2017	120	1782	51	758	29.4	1.3
1.2018	130	1912	55	813	31.9	1.4
2.2018	115	2027	49	861	42.3	1.9
3.2018	138	2165	59	920	40.7	1.8
4.2018	155	2320	66	986	36.1	1.6
5.2018	142	2461	60	1046	34.7	1.5
6.2018	160	2621	68	1114	39.0	1.7
7.2018	79	2700	34	1148	24.6	1.1

Table 4.2: Summary of irradiations for the chip A4W7G7R41.

4.1 The analysis of threshold and temporal noise

In case of ALPIDE, the charge threshold is the quantity of deposited charge, which is registered by pixels with 50 % probability. In ALPIDE sensor charge threshold is depend mainly on I_{THR}, which determine the shape of the pulse, and V_{CASN}, which regulates the baseline voltage [18]. With increasing I_{THR} the pulse height and width reduces, which leads to increase of charge threshold. On the other hand with increasing V_{CASN} baseline voltage increases and charge threshold reduces [1].

The measurement of the charge threshold and temporal noise is made by the following method: the same charge Q_{inj} is injected N times by a capacitance C_{inj} in a chosen pixel. After that the activation function $r(Q_{\text{inj}})$ is determined as follows:

$$r(Q_{\text{inj}}) = \frac{N_{\text{hit}}(Q_{\text{inj}})}{N}, \tag{4.1}$$

where $N_{\text{hit}}(Q_{\text{inj}})$ is the number of registered hits and N is the total number

of charge injections. Assuming the Gaussian distribution of the temporal noise, the activation function can be parametrized using the Error function as

$$\frac{1}{2}\left[1+\mathrm{erf}\left(\frac{Q_{\mathrm{inj}}-Q_{\mathrm{THR}}}{\sqrt{2}\sigma}\right)\right], \tag{4.2}$$

where erf is an error function, which accounts for the smearing of the threshold due to temporal noise, Q_{THR} is the charge needed to activate pixel with 50% probability and σ is a temporal noise. An example of experimentally obtained activation function is shown in Fig. 4.3. The curve is sometimes called the S-curve.

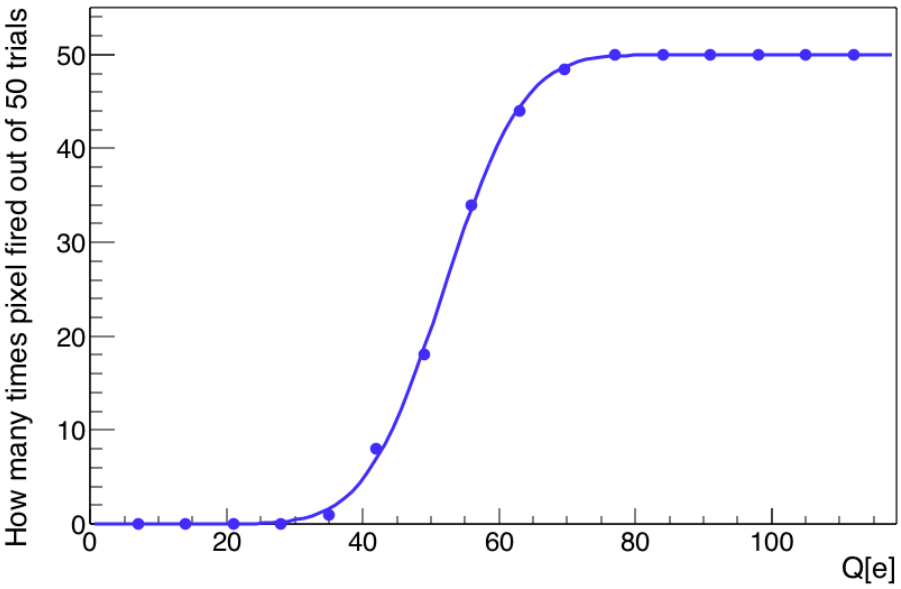

Figure 4.3: Example of activation function (S-curve) measured for one pixel of the sensor A4W7G7R41 as a function of Q_{inj}.

I have analyzed the measured activation functions on one chosen pixel in different time periods (for the chips A4W7G7R41 and A4W7G7R38 before the irradiations). The activation functions are shown in Fig.4.4, Fig.4.5. Let us point out that since the beginning of irradiations , the threshold was decreasing with the accumulated dose until the beginning of 2018, when the threshold was retuned by lowing VCASN. From Fig.4.4 and Fig.4.5 it is seen that in 2018 the activation function moved to the right, which means that threshold increased (the amount of charge needed for pixel activation increased). Nevertheless the width of activation region grows throughout all periods (temporal noise grows).

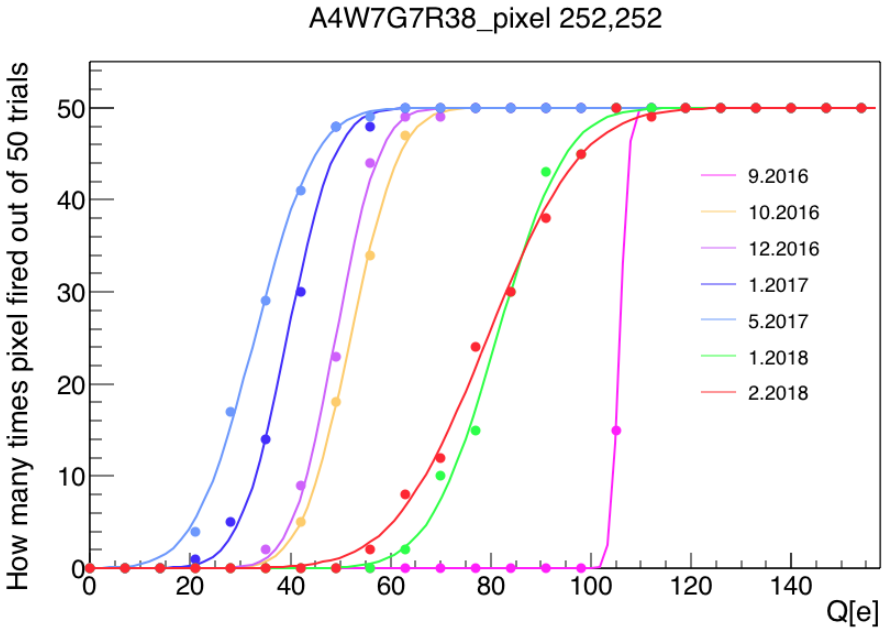

Figure 4.4: S-curve as a function of Q_{inj} of the chosen pixel [252,252] for the different time periods for chip A4W7G7R38. The curves for another time periods look similarly.

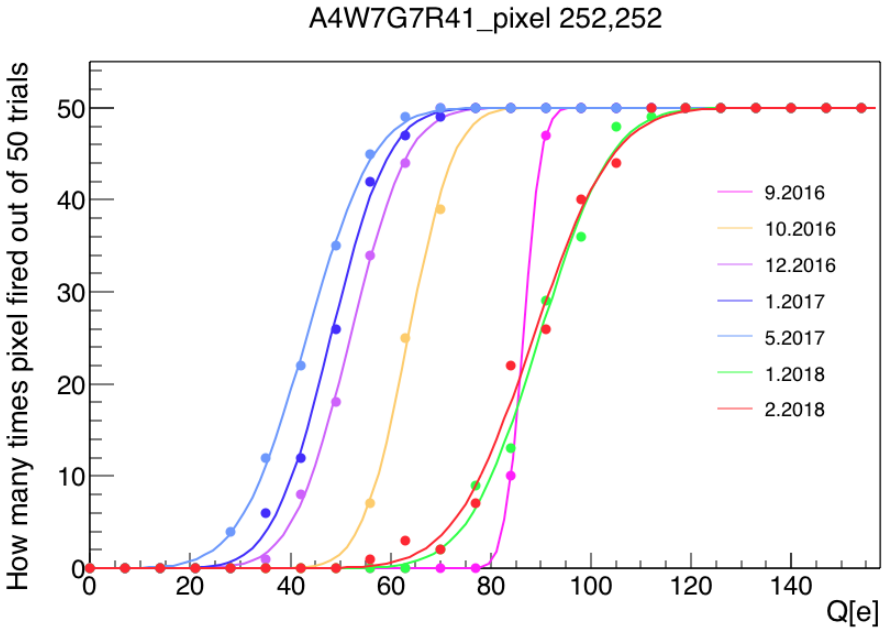

Figure 4.5: S-curve as a function of Q_{inj} of the chosen pixel [252,252] for the different time periods for chip A4W7G7R41. The curves for another time periods look similarly.

In Fig. 4.6 and 4.7 I present the dependence of the mean charge threshold on the accumulated dose. As can be seen from the figures, the mean threshold drops with increasing accumulated dose. However from November 2017 V_{CASN} settings were changed and threshold raised. After this change we also observe a visible effect of the annealing on the threshold (see Chapter 1.4.1). The new settings for VCASN however does not lead to a visible decrease of the average temporal noise which keeps rising. The noise keeps to decrease only during the annealing between irradiation campaigns.The dependences of temporal noise on total dose for both chips are shown in Fig. 4.8 and 4.9, the annealing process is manifested by a decline of the mean noise. Threshold and noise are measured in electron charges, dose in krad. In Fig. 4.10 and 4.11 is shown how does threshold in pixels change with the different V_{CASN}. With increasing V_{CASN} number of fired pixels decreases.

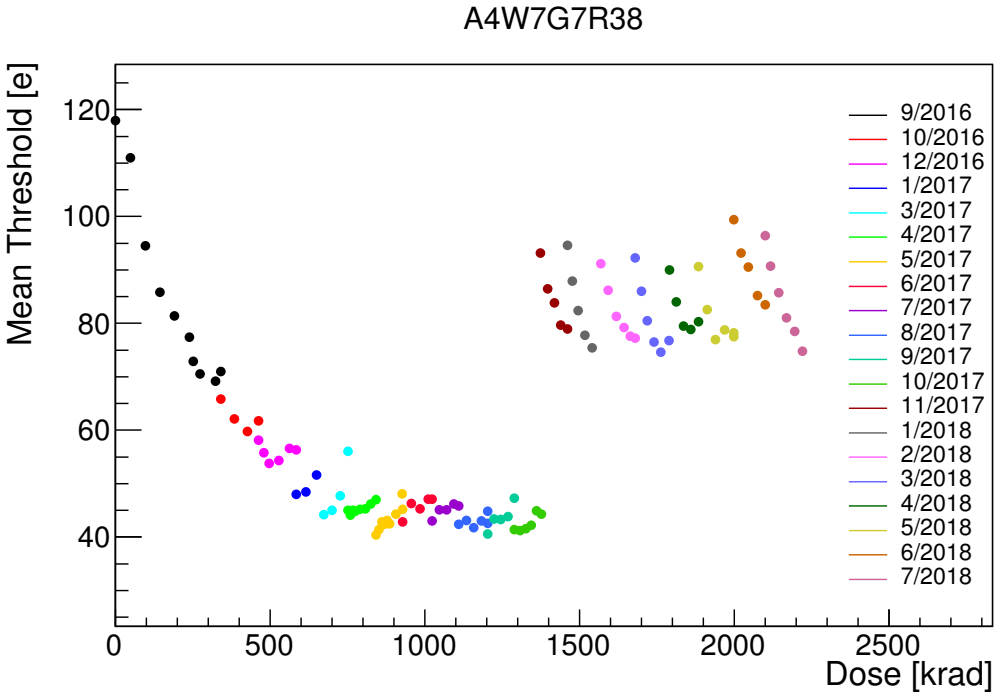

Figure 4.6: Mean threshold vs. accumulated dose for the chip A4W7G7R38.

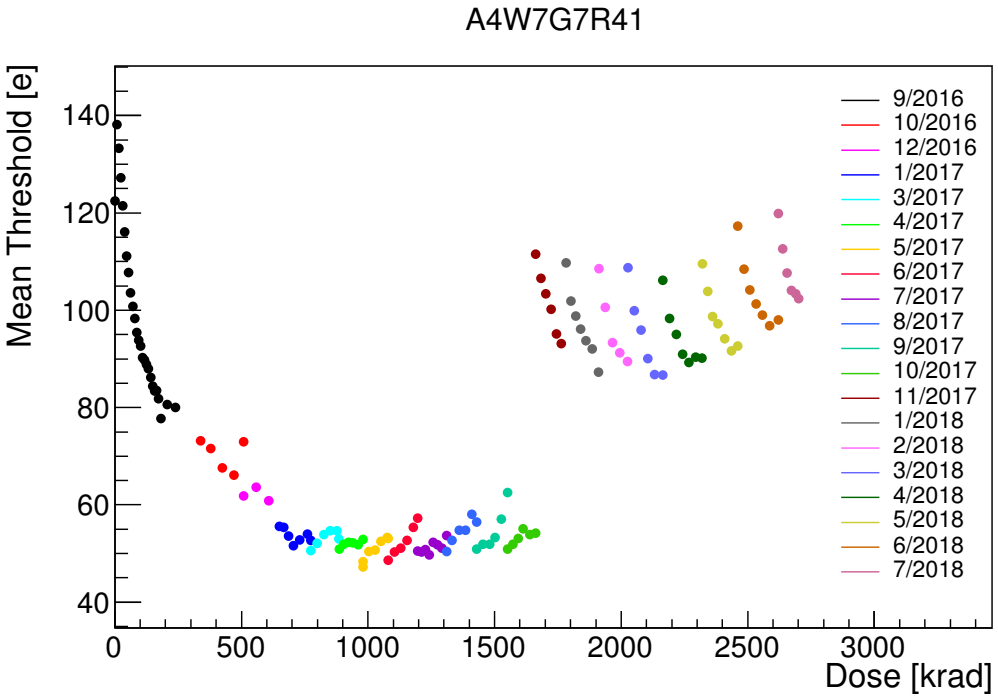

Figure 4.7: Mean threshold vs. accumulated dose for the chip A4W7G7R41.

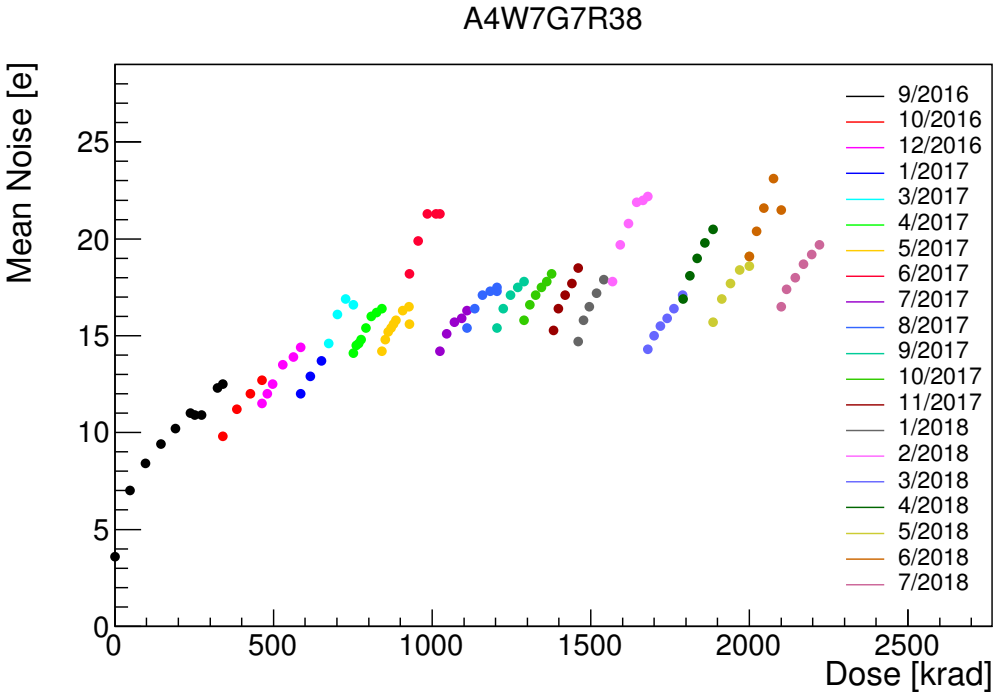

Figure 4.8: Mean noise vs. accumulated dose for the chip A4W7G7R38.

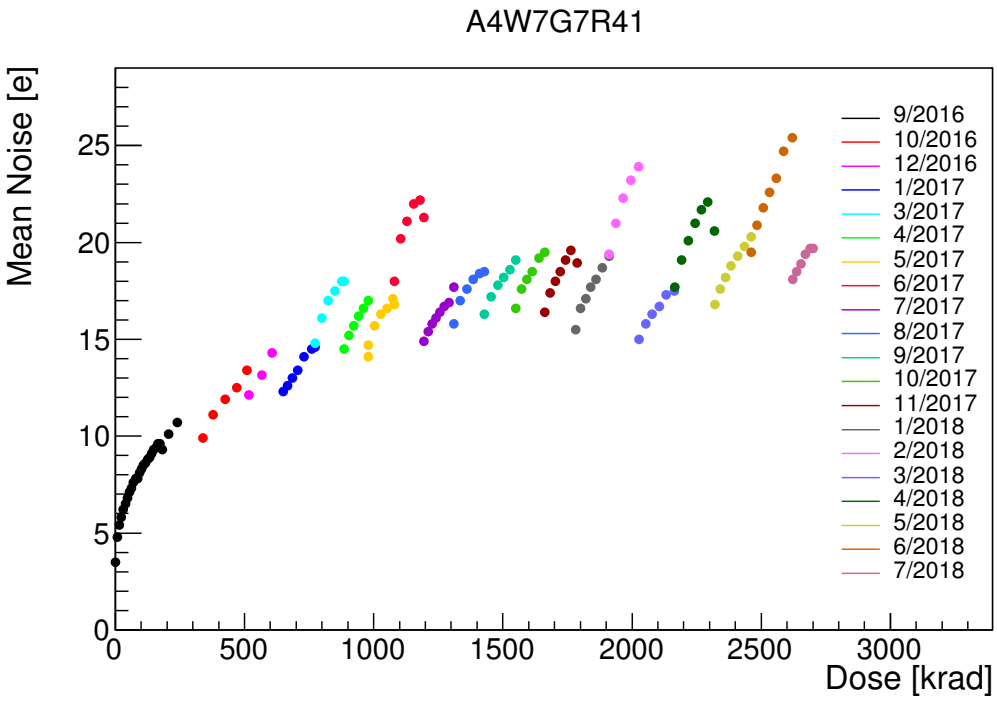

Figure 4.9: Mean noise vs. accumulated dose for the chip A4W7G7R41.

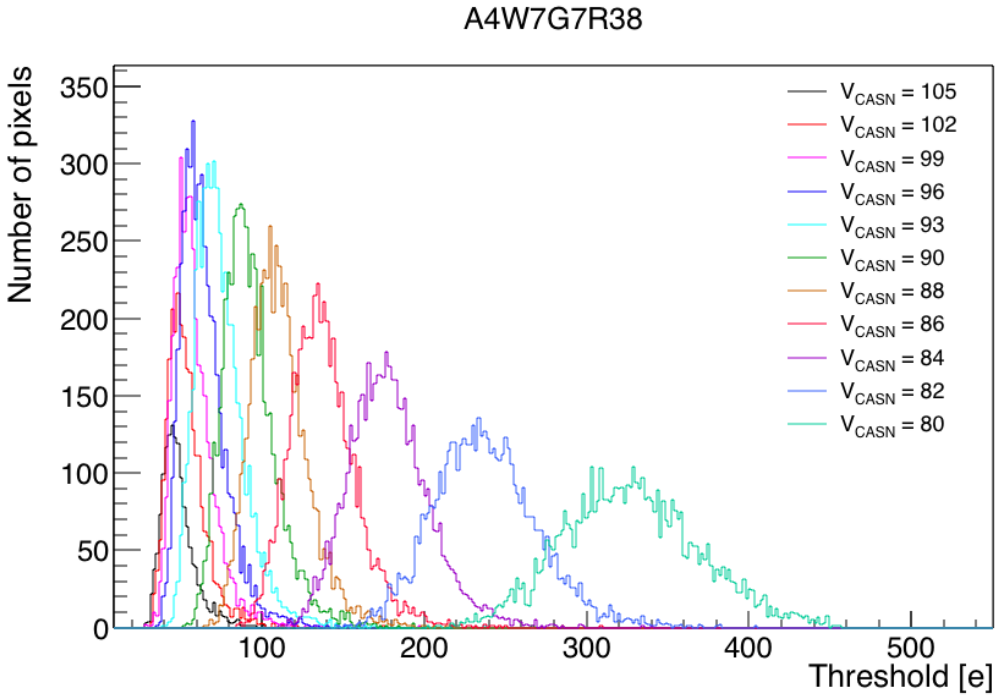

Figure 4.10: Distributions of charge threshold in pixels for different VCASN settings for the chip A4W7G7R38.

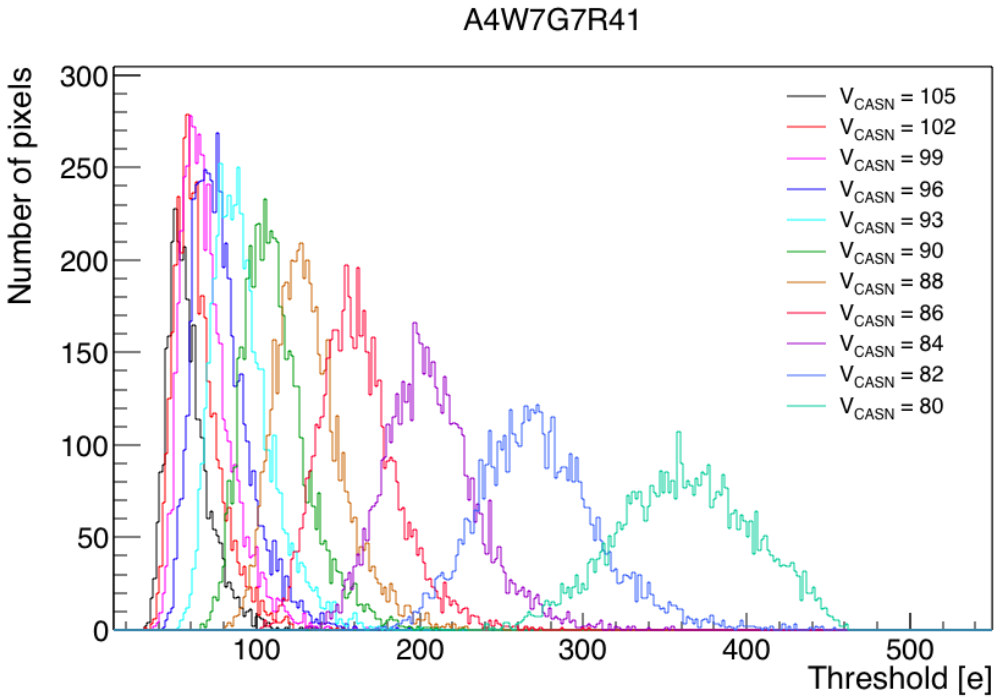

Figure 4.11: Distributions of charge threshold in pixels for different VCASN settings for the chip A4W7G7R41.

As was said before the most important parameters for threshold setting are I_{THR} and V_{CASN}. The dependences of those DAC parameters (scanned before each irradiation campaign) on accumulated dose are shown in Fig. 4.12, 4.13, 4.14 and 4.15. V_{CASN} has straight dependence during irradiation, while I_{THR} has linear dependence until the given DAC (working point of I_{THR} which sets the threshold, which is 51) value and then the linearity breaks down. $\mathrm{I_{THR}}$ shows annealing.

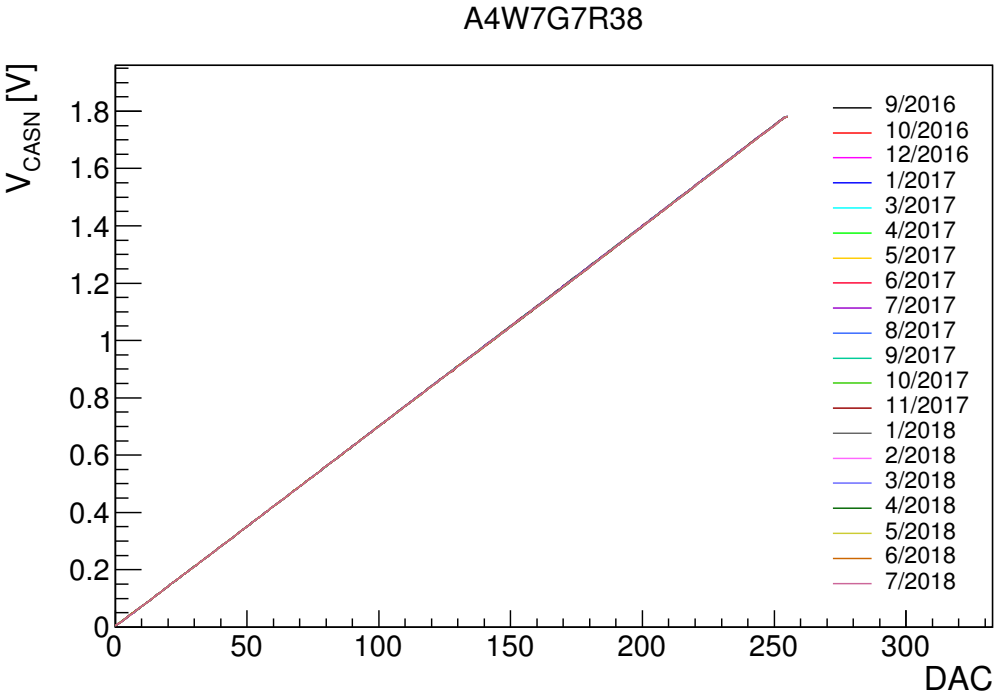

Figure 4.12: The dependence of V_{CASN} on DAC for chip A4W7G7R38.

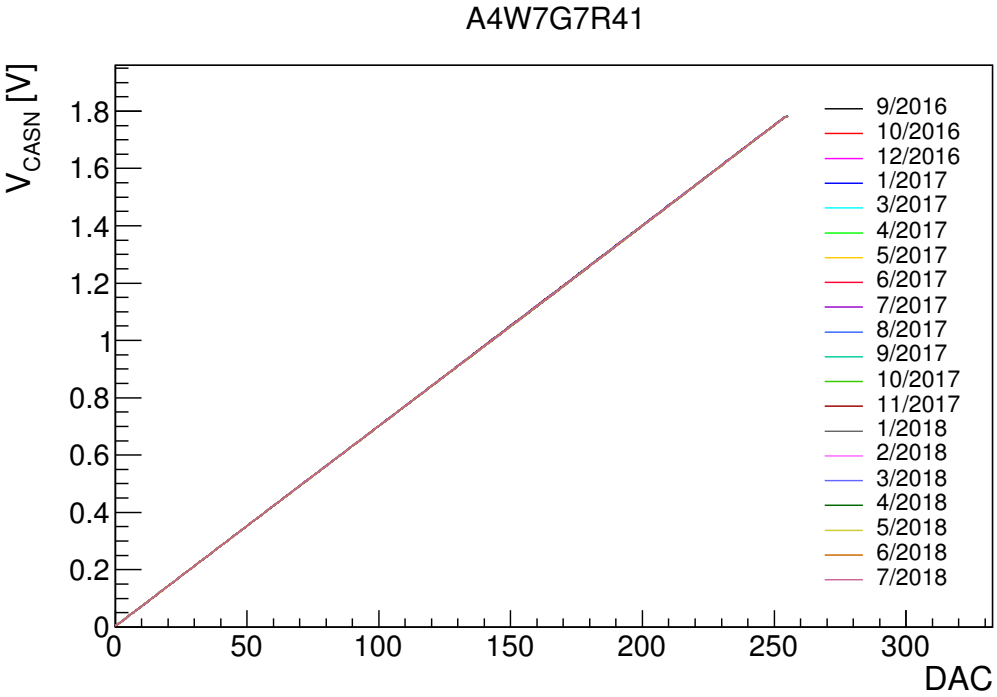

Figure 4.13: The dependence of V_{CASN} on DAC for chip A4W7G7R41.

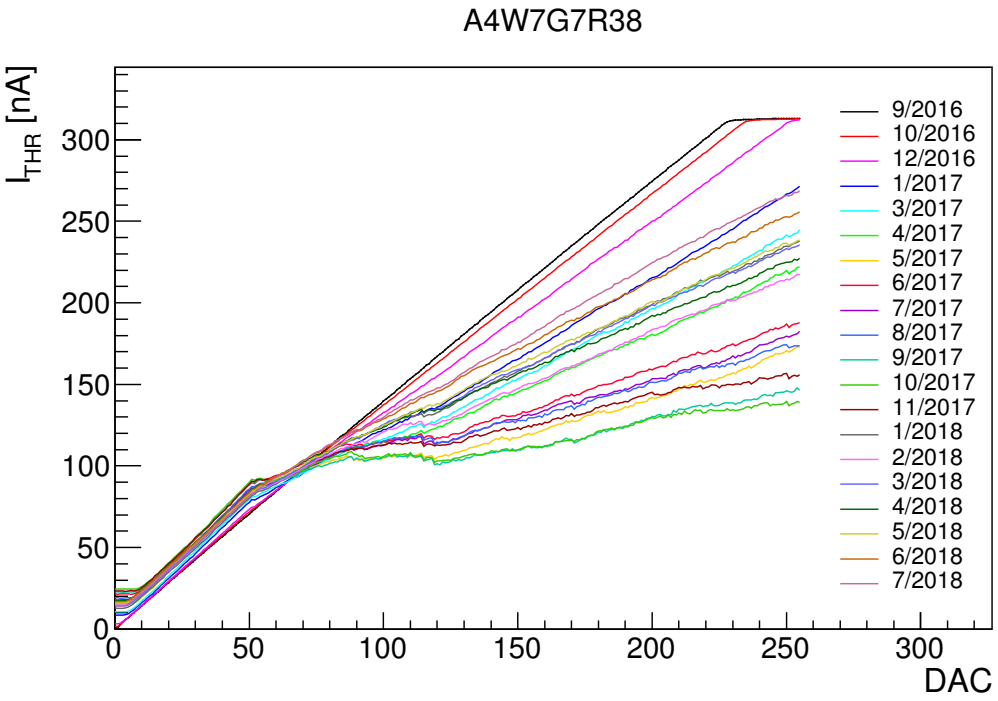

Figure 4.14: The dependence of I_{THR} on DAC for chip A4W7G7R38.

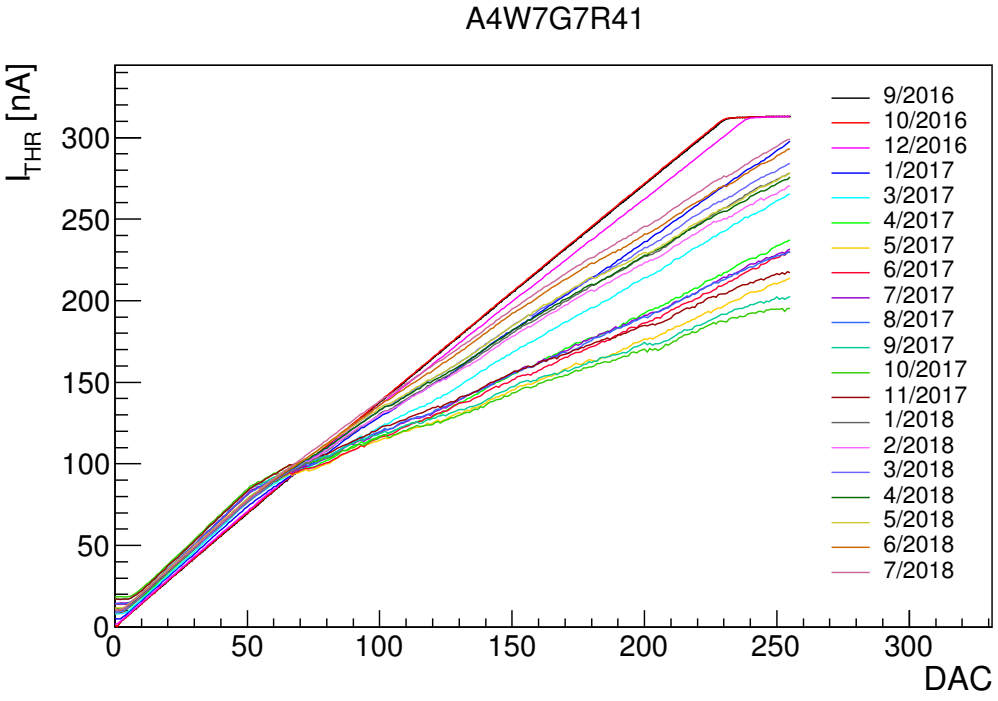

Figure 4.15: The dependence of I_{THR} on DAC for chip A4W7G7R41.

Conclusion

In this thesis, I deal with radiation hardness tests of the ALPIDE sensors. The ALPIDE sensors are intended to be used in the upgrade of the ALICE Inner Tracking System. Because the ALPIDE chip should sustain radiation loads up to 2700 krad, it is necessary to study its radiation hardness. Such tests were carried out at the U-120M cyclotron of the Nuclear Physics Institute of the Czech Academy of Sciences in Řež. The tests were performed for two chips, labeled A4W7G7R38 and A4W7G7R41. The status from July 2018 is the following: the chip A4W7G7R41 successfully sustained the requested radiation load however the accumulated dose for the second chip A4W7G7R38 is 2124 krad only. We see that on average the A4W7G7R38 was able to absorb less dose during irradiation campaigns than the chip A4W7G7R41. We expect that this behavior is a consequence of the different dose rates which were used for irradiation during the first campaign. Further we have seen that for the initial settings of the ALPIDE DACs, the mean threshold decreased with the total accumulated dose while the average temporal noise increased. After retuning of thresholds by applying the new VCASN settings in November 2017 we observe annealing of thresholds. The data from DAC scans show that the voltage DACs do not change with the accumulated dose and remain linear. On the other hand, the current DACs break their linearity above the usual working point. The original trend is never recovered and we see only partial recovery by annealing. The work on this project will continue with further irradiations of the chip A4W7G7R38 and we plan to characterize performance of the chip A4W7G7R41 using 6 GeV/c pion beam from the CERN PS. This study will show whether the chip still meets the project requirements in terms of detection efficiency and fake hit rate.

Literature

[1] K. Aamodt (ALICE collaboration), JINST 3 (2008) S08002

[2] Evans, L., Bryant, P. (editors), *LHC machine*, JINST 3 (2008), S08001.

[3] J. C. Collins and M. J. Perry, *Superdense matter: Neutrons or asymptotically free quarks?*Phys. Rev. Lett. , 34:1351356, May 1975.

[4] Edward V Shuryak, *Quantum chromodynamics and the theory of superdense matter.* Physics Reports , 61(2):71158, 1980.

[5] R. Stock, *Relativistic Nucleus-Nucleus Collisions and the QCD Matter Phase Diagram*, arXiv: 0807.1610v1 [nucl-ex]

[6] A. Majumder and M. Van Leeuwen, *The Theory and Phenomenology of Perturbative QCD*

[7] K. Aamodt et. al.(ALICE collaboration) *Phys. Rev. Lett.***105** 252301(2010)

[8] Abelev, B et al. (ALICE Collaboration), Technical Design Report for the Upgrade of the ALICE Inner Tracking System, J.Phys.G 41 (2014), 087002.

[9] ALICE, *Letter of intent*, J.Phys. G41 (2014) 087001

[10] *Upgrade of the ALICE Time Projection Chamber - ALICE Collaboration (Lippmann, Christian for the collaboration) CERN-LHCC-2013-020, ALICE-TDR-016*

[11] Antonioli, P (ed.) ; Kluge, A (ed.) ; Riegler, W (ed.), *Upgrade of the ALICE Readout Trigger System CERN-LHCC-2013-019; ALICE-TDR-015*

[12] ALICE general figures, `https://alice-figure.web.cern.ch/general_fig`, [Online 24.02.2018].

[13] W. R. Leo, *Techniques for Nuclear and Particle Physics Experiments*, 1987.

[14] G. Lutz, *Semiconductor Radiation Detectors, Chapter: Semiconductors as Detectors, str. 79-81*, 2007.

[15] Silicon electrical properties, `http://www.ioffe.ru/SVA/NSM/Semicond/Si/electric.html`, [Online 6.09.2018]

[16] Syed Naeem Ahmed, *Physics and Engineering of Radiation Detection*, 2007.

[17] H. Spieler, *Semiconductor Detector Systems*, Oxford University Press 2005.

[18] Jacobus Willem van Hoorne, *Study and Development of a novel Silicon Pixel Detector for the Upgrade of the ALICE Inner Tracking System*, PhD thesis, TU Vienna, Oct 2015.

[19] M. Moll, *Radiation damage in silicon particle detectors: Microscopic defects and macroscopic properties*, PhD thesis, Hamburg U., 1999.

[20] E. Fretwurst, G. Lindstrom, I. Pintilie and J. Stahl, *Radiation damage in silicon detectors caused by hadronic and electromagnetic irradiation*, arXiv preprint physics/0211118 (2002).

[21] Hartmut Hillemanns, *Radiation Hardness of Monolithic Active Pixel Sensors for the ALICE Inner Tracking System Upgrade*, CERN, CH-1211.

[22] Mónika Varga-Ko˝faragó, *Anomalous Broadening of Jet-Peak Shapes in Pb–Pb Collisions and Characterization of Monolithic Active Pixel Sensors for the ALICE Inner Tracking System Upgrade*, CERN-Thesis, 2018.

[23] Nuclear physics, MSU, `http://nuclphys.sinp.msu.ru/experiment/accelerators/ciclotron.htm`, [Online 22.07.2018].

[24] T. Matlocha, *Soustava pro vývod kladných iontů z cyklotronu,* Studie k disertační práci FJFI ČVUT, 2018.

[25] L.H. Thomas, *The Paths of Ions in the Cyclotron I. Orbits in the Magnetic Field* Phys. Rev. 54, 580 (1938).

[26] Department of accelerators, Isochronous cyclotron U-120M, [Online; accessed 19.05.2017].
`http://accs.ujf.cas.cz` .

[27] Center o fAccelerators and Nuclear Analytical Methods, Nuclear Physics Institute of the CAS, [Online; accessed 11.09.2018]. `http://canam.ujf.cas.cz` .

[28] T. Vaňát, *Physical Fault Injection and Monitoring Methods for Programmable Devices*, Disertační práce, FIT ČVUT 2017.

[29] F. Křížek, ... V. Raskina, ... , *Nuclear Inst. and Methods in Physics Research (NIM)*, A 894 (2018) 87–95.

[30] EQUIPCO. Introduction to radiation detectors, [Online; accessed 10.09.18] `https://www.equipcoservices.com/support/tutorials/introduction-to-radiation-monitors/`.

[31] User manual, *Ionization Chamber Type 30010, 30011, 30012, 30013; D596.131.00/03 2006-09 Hn*, Freiburg: PTW, 2013. 16.

[32] L. Musílek, *Úvod do fyziky ionizujícího záření*, SNTL 1979.

[33] UNIDOS E, Universal dosemeter, [Online; accessed 10.09.2018]. http://www.ptw.de/unidos_e_dosemeter_ad0.html .

[34] The LANG positioning system. MCL, [Online; accessed 10.09.18] http://www.lang.de/de/produktbereiche/automations-systeme/positioniersysteme/mcl.html?tx_wtgallery_pi1$%$5Bshow$%$5D=66135039&cHash=6dc210ed04b37c56c7096c4df16b7534 .

[35] James F. Ziegler, Jochen P. Biersack, *The Stopping and Range of Ions in Matter.*, editor, Treatise on Heavy-Ion Science, pages 93–129. Springer US, 1985

[36] V. Raskina, *Measurement of proton flux from the U-120M cyclotron using activation foils*, Bakalářská práce, FJFI ČVUT 2018.

[37] K. Vysoká, *Low Proton Flux Measurements at the U-120M Cyclotron for Radiation Hardness Studies*, Master's thesis, FJFI ČVUT 2016.

[38] ESCC, *Single event effects tests method and guidelines*, ESCC Basic Specification No. 25100, October 2016.

Appendix

Appendix A

Dose calculation

Total ionizing dose D is estimated by formula:

$$D[\text{krad}] = 1.602 \times 10^{-8} \times \text{LET}[\text{MeV} \cdot \text{cm}^2 \cdot \text{mg}^{-1}] \times F[\text{cm}^{-2}], \tag{A.1}$$

where LET is the stopping power, F is fluence. The unit test may be made in the following way. The effective unit of LET$\times F$ is $1\frac{\text{MeV}}{\text{mg}}$, which can be written as

$$1\frac{\text{MeV}}{\text{mg}} = \frac{10^{-6}\text{eV}}{10^{-6}\text{kg}} = 10^{12}\frac{\text{eV}}{\text{kg}} = 10^{12} \cdot \frac{e \cdot J}{\text{kg}} = 10^{12} \cdot e \cdot \text{Gy}, \tag{A.2}$$

where e is elementary charge and 1 Gy = 0.1 krad. Which leads to

$$1\frac{\text{MeV}}{\text{mg}} = 10^{12} \cdot e \cdot 0.1 \text{ krad} = 10^{11} \cdot e \cdot \text{krad} = 1.602 \cdot 10^{-8}\text{krad},$$

$$1\frac{\text{MeV}}{\text{mg}} = 1.602 \cdot 10^{-8}\text{krad}. \tag{A.3}$$

It means that if we measure LET$\times F$ in $1\frac{\text{MeV}}{\text{mg}}$, we should multiply it by factor $1.602 \cdot 10^{-8}$ to get krad.